

# Topographic thresholds for gully head formation in badlands

Mauro Rossi<sup>1</sup>  | Dino Torri<sup>1</sup> | Sofie De Geeter<sup>2</sup> | Cati Cremer<sup>2</sup> | Jean Poesen<sup>2,3</sup>

<sup>1</sup>Istituto di Ricerca per la Protezione Idrogeologica, Consiglio Nazionale delle Ricerche, Perugia, Italy

<sup>2</sup>Department of Earth and Environmental Sciences, KU Leuven, Heverlee, Belgium

<sup>3</sup>Institute of Earth and Environmental Sciences, UMCS, Lublin, Poland

## Correspondence

Mauro Rossi, Istituto di Ricerca per la Protezione Idrogeologica, Consiglio Nazionale delle Ricerche, Via Della Madonna Alta 126, 06128 Perugia, Italy.  
 Email: [mauro.rossi@irpi.cnr.it](mailto:mauro.rossi@irpi.cnr.it)

## Funding information

KU Leuven; CNR\_IRPI

## Abstract

Gully erosion is a particularly damaging process which is not yet sufficiently understood and parameterized. Gully head topographic threshold relative to Hortonian runoff have been studied in cropland, rangeland and forest. This study extends such modelling approach to badlands. Different badlands (eight sites) have been studied in the Mediterranean environment in Italy and Spain, characterized by diversified climatic, lithological, and geological settings under different anthropogenic conditioning. Many badlands have been characterized by their specific human history in addition to their geomorphological properties. Land use, as part of the human history, strongly affected many badland formation and development, through extremely impacting land exploitation (usually overgrazing). The effect of geological and geomorphological processes are usually particularly well visible. While the weakening effect of joints is confirmed, the different geological layer bedding orientation with respect to the slope aspect generates a different development of badland morphologies and different values of gully head thresholds values (as shown in two badlands sites on the same geological material and climate).

The selection of Curve Number values, at the base of the introduction of land use into the gully head thresholds, has been more objectively defined in order to reduce arbitrariness in threshold application. The study additionally revises some of the physical basics behind the gully head threshold concept, requiring a description of the soil resistance in terms of frictional and cohesive components. This implies the explicit inclusion of rock fragment into the grain size distribution, which cannot be limited to fine grains. It results into an enriched threshold formulation that allows to describe the condition for gully head initiation and retreat as the result of the tradeoff between the frictional and cohesive components of the soil resistance forces. Eventually, the gully head threshold concept is confirmed and extended to include badlands.

## KEY WORDS

badlands, critical runoff shear stress, Curve Number, geological setting, grain friction angle, gully head threshold, rock fragments, soil cohesion, soil resistance

## 1 | INTRODUCTION AND THEORETICAL BACKGROUND

Gully development is a particularly damaging erosion process which is not yet sufficiently well understood and parameterized (Poesen et al., 2011). It can lead to badland development requiring intense topographic reshaping to remove gully channels and prevent the

formation of new channels. Evidently, land use, slope gradient, soil and the underneath geological layers with their characteristics and those inherited by the local orogenetic processes (e.g., joints and faults) contribute to the resistance offered by the land to the erosional potential of concentrated overland flow.

Gully channels extend over lengths that can be measured in metres up to kilometres, with widths spanning over tens of metres to

This is an open access article under the terms of the [Creative Commons Attribution](#) License, which permits use, distribution and reproduction in any medium, provided the original work is properly cited.

© 2022 The Authors. *Earth Surface Processes and Landforms* published by John Wiley & Sons Ltd.

less than one and depths ranging from a few centimetres (e.g., ephemeral summer gullies, Nachergeale et al., 2002) to tens of metres (e.g., Radoane et al., 1995; Poesen et al., 2003). Gullies occur in soils with a large textural range. Possible effects of soil texture on gully channel initiation and development have been observed and discussed in the literature (Radoane et al., 1995; Shahrivar & Christopher, 2012; Valentin et al., 2005). Evidently, a deep gully can erode by subsurface flow, seepage, piping and tunnel erosion, which can undercut more resistant top layers such as those colonized by plant roots (De Baets et al., 2008). Furthermore, tension cracks develop easily on vertical walls (particularly those of recently formed gully channels) which facilitate mass movements, leading to a change in slope gradient of the new channel walls towards gradients evolving towards the typical repose angle of the material. Lithology and its features may also strongly influence gully locations and patterns, particularly lithological layer bedding and orientation whereas density of joints may control drainage network, preferential flows and in turn surface and subsurface erosion (Beavis, 2000; Colica & Guasparri, 1990; Parkner et al., 2007). Soil material with its organic matter content (especially glomalin; Rillig & Mumey, 2006) makes soil aggregates more resistant to degradation and the pore system better structured for diffusing water into the soil profile. Also plant roots add to the soil resistance (Gyssels et al., 2005; De Baets et al., 2007). Subsurface flow can complement soil erosion by overland flow, resulting in a further upslope retreat of the gully head (GH). The more resistant top layer can reduce GH retreat rate. Despite important advances in understanding gully erosion processes over the last decades, predicting gully erosion still remains a major challenge (Poesen, 2017; Vanmaercke et al., 2021).

Mapping gullies, particularly over large areas, is time consuming and requires extensive field surveys. During the last decades, diverse methods have been applied to map gullies and their characteristics using manual (Bocco & Valenzuela, 1993; Fiorucci et al., 2015; Pérez & García, 2017), semiautomatic (Mararakanye & Nethengwe, 2012; Shruthi et al., 2011) or automatic methods and exploiting very high-resolution remote sensing (James et al., 2007; Vrielink et al., 2007), proximal sensing (Doumit & Awad, 2019) or close range data (Frankl et al., 2015). In addition, a growing body of literature is focused on diversified statistical approaches (i.e., from bi-variate to machine learning) to estimate susceptibility of study areas to gullyling (e.g., Conoscenti et al., 2013).

Despite large efforts made to map gullies and gully susceptibility, dealing with all the gully subprocesses remains difficult because of their interactions and because it is difficult to obtain adequate instrumentation to cover all possible field conditions (Poesen et al., 2011). Nevertheless, several models have been developed during the past 50 years. The empirical line that spans from the pioneering works of Beer and Johnson (1965) and Seginer (1966) to the recent review by Vanmaercke et al. (2016) suggests that rainfall intensity (average, maximum) and catchment area are two important factors for estimating GH retreat rates. More sophisticated models, such as those presented by Sidorchuk (1998, 1999, 2005, 2006) with the dynamic, static, deterministic and stochastic modelling of gullies, or by De Ploey (1992), Willgoose (2005), Tucker et al. (2001), Campo-Bescos et al. (2013) and Torri and Poesen (2014), have been developed, based on a strong or a semi-empirical physical base. These models introduce parameters which are difficult to extract from public databases or time-consuming and costly to determine for each case study. The GH

threshold model, introduced by Patton and Schumm (1975), refined by Montgomery and Dietrich (1994) and further expanded by Torri and Poesen (2014) to include land use, falls midway between a totally empirical and a physically-based approach. Such model predicts where GHs will form and then subsequently may retreat further upslope. Such sites in the landscape are described as a function of the local soil slope gradient at the GH, the surface area draining into it and the land use expressed through the maximum potential runoff production (which is predicted by the runoff Curve Number (CN); Hawkins et al., 2009). Next, rock fragment content in the topsoil, presence of joints (faults) and piping susceptibility are other (secondary) factors which help improving the prediction of the landscape position where a gully channel may form and retreat. This approach allows land-use types, such as rangeland, pasture, cropland and forest to be considered in the evaluation of the probability that a GH will be observed in a given landscape location.

Given the relatively simple data required for running the model proposed by Torri and Poesen (2014), it is worthwhile to further improve and expand this model to other land-use types. The dataset on which this model is based, contains field observations on GHs made in every continent and for several land-use types, including forest, rangeland, and cropland. Badlands were not included yet, despite the fact that they typically have a high gully density (e.g., Joshi, 2014; Joshi & Nagare, 2013; Torri, Poesen, et al., 2018). The Torri, Poesen, et al. (2018) study covers a Plio-Pleistocene marine sediment, silty clay, not cemented and over-consolidated, revealing two topographic threshold values, due to small differences in management for the same land use (overgrazed rangeland).

Given the scarce data on GHs in these environments, this study aims to better understand GH formation in badland-type environments by expanding the GH database for badlands that developed in other lithological and geological settings. Study sites have been selected in such a way that they are all located in a similar climatic zone, defined following the Köppen–Geiger classification as Mediterranean Cs type (see Table 1 for details on symbols and acronyms), in order to allow for the study of meteorological differences, without mixing their effects with climatic effects. Study sites were therefore selected in Italian and Spanish Mediterranean regions where badlands are common landscape features.

The study additionally explores the possible differences in gully occurrence between different badlands.

The study focus is on GH thresholds following the standardized methodology proposed by Torri and Poesen (2014) and revised by Torri, Poesen, et al. (2018) in order to avoid the risk of producing biased trends for topographic thresholds (Rossi et al., 2015). The study will also investigate the contribution of soil rock fragment content to the processes linked to the resistance to GH retreat (Torri & Poesen, 2014).

To address all these items in a coherent way, this article (i) presents the theoretical framework behind the topographic threshold concept, (ii) compares this with field observations collected during this study, (iii) identifies the shortcomings of such a theoretical framework, and finally (iv) proposes a generalization of the theory to account also for gullies in badlands.

## 1.1 | Gully head threshold theoretical background

This paragraph summarizes the physics behind the gully-head threshold model, its empirical components, weaknesses and aspects to be

**TABLE 1** Symbols and acronyms used in the text, with descriptions, units of measure and references for a more detailed information

Symbol/acronym	Type	Description	Unit of measure	Reference
T	Climate index	Average monthly air temperature	°C	
P	Climate index	Average monthly precipitation depth	mm	Grieser, 2006
PET	Climate index	Potential evapotranspiration	mm	CCI/CLIVAR/JCOMM Expert Team on Climate Change Detection and Indices (ETCCDI), 2020; Frich et al., 2002;
SU	Climate index	Number of days in a year with daily maximum temperature > 25°C (Summer days)	days	Zhang et al., 2011
TN/TR	Climate index	Number of days in a year with daily minimum temperature > 20°C (Tropical nights)	days	
R10	Climate index	Number of days in a year with daily precipitation > 10 mm	days	
RR1	Climate index	Number of days in a year with daily precipitation > 1 mm	days	
PRCPTOT	Climate index	Cumulative precipitation for days with daily precipitation > 1 mm in a year	mm	
PRCPTOT_DJF	Climate index	Cumulative precipitation for days with daily precipitation > 1 mm in the winter season (D: December, J: January, F: February)	mm	
PRCPTOT_MAM	Climate index	Cumulative precipitation for days with daily precipitation > 1 mm in the spring season (M: March, A: April, M: May)	mm	
PRCPTOT_JJA	Climate index	Cumulative precipitation for days with daily precipitation > 1 mm in the summer season (J: June, J: July, A: August)	mm	
PRCPTOT SON	Climate index	Cumulative precipitation for days with daily precipitation > 1 mm in the autumn season (S: September, O: October, N: November)	mm	
PRCPTOTX_SEASON	Climate index	Maximum quarterly (seasonal) cumulative precipitation for days with daily precipitation > 1 mm in the autumn season (this index is a modified version of the previous four indices proposed in this study)	mm	
PRCPTOTX_MONTHS	Climate index	Quarterly period corresponding to PRCPTOTX_SEASON	mm	
RX1DAY	Climate index	Maximum daily precipitation in a year	mm	
SDRR	Climate index	Number of snow days in a year. A snow day has daily precipitation > 1 and average daily air temperature ≤ 2	days	
R95pTOT	Climate index	Total precipitation depth during very wet days (Rain > 95th percentile)	mm	
R99pTOT	Climate index	Precipitation total due to extremely wet days (Rain > 95th percentile)	mm	
RDN	Climate index	Rainy Day Normal is calculated as RDN = PRCPTOT/RRR	mm/d	
AI DM	Climate index	Annual De Martonne Aridity Index	mm/°C	Baltas, 2007; de Martonne, 1942; Tabari et al., 2014
AI DM_MM	Climate index	Driest month De Martonne Aridity Index	mm/°C	

(Continues)

TABLE 1 (Continued)

Symbol/acronym	Type	Description	Unit of measure	Reference
AP	Climate index	De Martonne Combinative Index	mm/°C	
ZJ	Site code	Zarzuela de Jadraque	n.a.	
VJ	Site code	Villares de Jadraque	n.a.	
HE	Site code	Hiedelaencina	n.a.	
PV	Site code	Puebla de Valles	n.a.	
LB	Site code	Leonina Biancana	n.a.	
LH	Site code	Leonina Hillslope	n.a.	
VR	Site code	Verghereto	n.a.	
MN	Site code	Montione	n.a.	
TPS	Acronym	Total Station Positioning System	n.a.	
GNSS	Acronym	Global Navigation Satellite System	n.a.	
RTK	Acronym	Real-Time Kinematic correction	n.a.	
GH	Acronym	Gully/head	n.a.	
A	Process variable	Area draining into the gully head	ha	
$\vec{c},  \vec{c} , c$	Process variable	Soil cohesion vector and relative intensity/modulus	Pa	
C	Process variable	Clay fraction	dimensionless	Smerdon & Beasley, 1959, 1961
$\bar{F}_{\text{stress}}$	Process variable	Fluid stress	Pa	
$F_{\text{Statio}}$	Process variable	the ratio ( $F_{\text{Statio}}$ ) between average fluid stress ( $F_{\text{stress}}$ ) and average soil resistance ( $\bar{R}_{\text{soil}}$ )	dimensionless	Torri et al., 1987
g	Process variable	Acceleration due to gravity	m/s <sup>2</sup>	
h	Process variable	Flow depth or hydraulic radius	m	
$h_f$	Process variable	Fraction of grain submerged	dimensionless	
I	Process variable	Infiltration rate	m/s	
k	Process variable	Coefficient expressing the resistance of a site to gully head retreat, calculated from field data using $k = \sin(\gamma)/A^{0.4}$	ha <sup>0.4</sup>	
$k_{1st}$	Process variable	First percentile of the observed distribution of k values	dimensionless	
$k_{ratio}$	Process variable	Ratio between $k_{1st}$ observed and $k_{1st}$ calculated	dimensionless	
$k_u$	Process variable	Empirical scaling constant linking fluid velocity to discharge	$m^{(1-3\beta)} s^{(\beta-1)}$	Govers et al., 2000; Nearing et al., 1999
$k_w$	Process variable	Empirical constant for channel width used for synthetically represent other constants	$(m^{-3} s)^{0.534} m$	
u	Process variable	Manning's hydraulic roughness	s/m	
P	Process variable	Daily precipitation	mm	USDA & NRCS, 2019
$P_a$	Process variable	Annual precipitation	mm	

(Continues)

TABLE 1 (Continued)

Symbol/acronym	Type	Description	Unit of measure	Reference
$Q_{CN}$	Process variable	Runoff density (volume per unit area)	mm	USDA & NRCS, 2019
$Q$	Process variable	Runoff discharge	$\text{m}^3/\text{s}$	
$Q_o$	Process variable	Empirical constant with the dimension of a discharge	$\text{m}^3/\text{s}$	Pilar Salvador Sanchis et al., 2009
$R$	Process variable	Rain intensity	$\text{m}/\text{s}$	
$\vec{R}$	Process variable	Soil frictional resistance vector	Pa	
$\bar{R}_{\text{soil}}$	Process variable	Average soil resistance	Pa	
$\vec{R}_{\text{tot}}$	Process variable	Total soil resistance vector, including frictional and cohesive resistance forces and gravity. This represents the total force acting over a soil grain without the fluid stresses.	Pa	
$ \vec{R}_{\text{tot}} , R_{\text{tot}}, R,  \vec{R} $	Process variable	Intensity or modulus of the corresponding vectors	Pa	
$R_x$	Process variable	Component on soil frictional resistance parallel to the slope	Pa	
$R_z$	Process variable	Component on soil frictional resistance normal to the slope	Pa	
RCF	Process variable	Rock fragment content/cover	dimensionless	
$S_{d,49}$	Process variable	Standard deviation of the friction angle distribution	rad or deg	
$S_h, S_{0.2}, S_{0.05}$	Process variable	Maximum potential rain losses	mm	Hawkins et al., 2009; USDA & NRCS, 2019
$S_y$	Process variable	Sediment yield	$\text{Mg km}^{-2} \text{a}^{-1}$	Langbein & Schumm (1958)
$u$	Process variable	mean flow velocity	$\text{m s}^{-1}$	
$V_c$	Process variable	Vegetation cover	dimensionless	USDA & NRCS, 2019
$W$	Process variable	Fluid stream power per unit of volume	$\text{W m}^{-3}$	Torri et al., 2012
$W_{cr}$	Process variable	Critical value of fluid stream power per unit of volume to induce the gully head to retreat further	$\text{W m}^{-3}$	Torri & Poesen, 2014
$w$	Process variable	Channel width (transverse to flow direction) covered by the channeled/channelling fluid	m	
$\alpha$	Process variable	Empirical exponent of the Leopold and Maddock extended equation for channel width	dimensionless	Pilar Salvador Sanchis et al., 2009
$\beta$	Process variable	Empirical exponent	dimensionless	Govers et al., 2000; Nearing et al., 1999
$\zeta$	Process variable	Diameter of the grain normal to the soil surface	m	
$\gamma$	Process variable	Local gradient	rad or deg	
$\psi$	Process variable	Factor accounting for local conditions affecting gully topographic thresholds (originally written as c)	dimensionless	Torri & Poesen, 2014
$\rho_f$	Process variable	fluid density	$\text{kg/m}^3$	
$\rho_s$	Process variable	Saturated soil grain density	$\text{kg/m}^3$	
$\tau_e$	Process variable	Critical value of the fluid shear stresses required to equal the soil/ecosystem resistance	Pa	

(Continues)

TABLE 1 (Continued)

Symbol/acronym	Type	Description	Unit of measure	Reference
$\tau_f$	Process variable	flow shear stress or bottom flow shear stress	Pa	
$\varphi$	Process variable	Friction angle	rad or deg	
$\varphi_{50}$	Process variable	The 50th percentile of the friction angle distribution	rad or deg	
$\varphi_{80}$	Process variable	The 80th percentile of the friction angle distribution	rad or deg	
$\chi$	Process variable	Proportionality coefficient for the extended Leopold and Maddock equation for channel width	m	Pilar Salvador Sanchis et al., 2009

Note: n.a., not available.

further developed. Montgomery and Dietrich (1994) proposed the basic inequality (Equation 1). Table 1 summarizes all symbols and acronyms used in the text later, providing a proper description and specifying the units of measure and references for more detailed information.

Rossi et al. (2015) and Torri and Poesen (2014) reviewed GH thresholds studies relative to Hortonian overland flow introducing an empirical component based on the USDA and NRCS (2019) CN method. Later Torri, Poesen, et al. (2018) expanded the observed range of land-use types with GHs to include one badland site. Furthermore, they proposed a modification of the basic equations in order to avoid problems for areas that have low CN values.

The threshold concept for GH formation which then retreats further upslope derives from the fact that concentrated overland flow should exert flow shear stresses in excess of a critical value to erode the soil. This critical flow shear stress is the value at which the most resistant fraction of the soil material is entrained by the flow and either wall or bed armouring is impeded. This condition should last long enough to allow the flow at the GH to cut a cross-sectional area exceeding a critical value (Hauge, 1977; Poesen et al. 2003). Montgomery and Dietrich (1994) noted that the flow shear stress ( $\tau_f$ ) produced by runoff must exceed a critical threshold value ( $\tau_{cr}$  expressed in pascals) to erode a gully channel. Hence, it follows:

$$\tau_f = \rho_f g h \sin \gamma \geq \tau_{cr} \quad (1)$$

where  $\rho_f$  is the fluid density measured in kg/m<sup>3</sup>,  $g$  is acceleration due to gravity in m/s<sup>2</sup>,  $h$  is flow depth (or hydraulic radius) measured in metres, and  $\gamma$  is slope angle of the soil surface.

Considering that:

$$Q = u h w = \frac{1}{n} w h^{5/3} \sin(\gamma)^{1/2} \quad (2)$$

where  $Q$  is flow discharge rate measured in m<sup>3</sup>/s,  $u$  is mean flow velocity measured in m/s,  $w$  is the width of the channel head measured in metres,  $n$  is Manning's hydraulic roughness coefficient expressed in s/m<sup>1/3</sup>.

According to Montgomery and Dietrich (1994), the discharge rate  $Q$ , which assumes that the entire upslope catchment area  $A$  contributes to the overland flow (i.e., when depression storage is filled, hence  $R > I$ ), is given by:

$$Q = (R - I) \cdot A \quad (3)$$

where  $R$  is rainfall intensity and  $I$  is infiltration capacity, both expressed in m/s, and  $A$  is measured in m<sup>2</sup>.

Then, resolving Equation (2) for  $h$  and using Equation (3), it follows:

$$h = \left[ \frac{n(R - I)A}{w} \right]^{3/5} \sin(\gamma)^{-3/10} \quad (4)$$

Substituting Equation (4) for  $h$  into Equation (1) it follows:

$$\tau_f = g \rho_f \sin \gamma \left[ \frac{n(R - I)A}{w} \right]^{3/5} \sin(\gamma)^{-3/10} \geq \tau_{cr} \quad (5)$$

Now, with a few re-arrangements we obtain:

$$\sin \gamma^{\frac{1}{10}} \left[ \frac{n(R-I)A}{w} \right]^{\frac{3}{5}} \geq \frac{\tau_{cr}}{g\rho_f} \quad (6)$$

Any channel width can be estimated by an extension of the Leopold and Maddock equation as rewritten by Pilar Salvador Sanchis et al. (2009):

$$w = \chi \left( \frac{Q}{Q_0} \right)^\alpha \quad (7)$$

where  $\chi$  (measured in metres) and  $Q_0$  (in  $m^3/s$ ) are empirical constants and  $\alpha = 0.534 \cdot (1 - 0.345e^{-2.55w})$ . For  $w \geq 0.8 m$  the exponent becomes constant (see figure 2 in Pilar Salvador Sanchis et al., 2009) and Equation (7) becomes:

$$w = k_w Q^{0.534} \text{ with } k_w = \frac{\chi}{Q_0^{0.534}} \quad (8)$$

where  $k_w$  is an empirical coefficient (Pilar Salvador Sanchis et al., 2009).

Introducing Equation (8) into Equation (6) we obtain:

$$\sin \gamma^{\frac{1}{10}} \left[ n(R-I) \frac{A^{0.466}}{k_w(R-I)^{0.534}} \right]^{\frac{3}{5}} \geq \frac{\tau_{cr}}{g\rho_f} \quad (9)$$

and

$$\sin \gamma A^{0.4} > k \text{ with } k = \left[ \frac{k_w^{0.6} \tau_{cr}}{g\rho_f n^{0.6} (R-I)^{0.28}} \right]^{\frac{10}{7}} \quad (10)$$

with  $k$  (reflecting the resistance of a site to gully development) is a coefficient accounting for several factors, some of which relate to the soil resistance (e.g.,  $\tau_{cr}$ ) and others relate to flow erosivity (e.g.,  $R-I$ ). Despite this relation is supported by the literature (this is substantially derived from equation (7) in Montgomery and Dietrich, 1994), there are still parameter interdependencies to be explored. For instance,  $k$  decreases with increasing hydraulic roughness ( $n$ ), which is counterintuitive. This apparent inconsistency is due to the fact that in Equation (10), the physical threshold is  $\tau_{cr}$  while  $k$  is a dummy constant used to simplify a multi-dimensional threshold into a two dimensional one. Other approaches removed this apparent inconsistency, but introduced less well-established empirical equations.

An alternative  $k$  formulation can be based on the stream power per unit of volume  $W$  in  $W/m^3$  (SI system; Torri et al., 2012):

$$W = u \rho_f g \sin \gamma \quad (11)$$

where  $u$  is mean flow velocity, which in sediment laden flows depends only on discharge:

$$u = k_u Q^\beta \quad (12)$$

where  $k_u$  and  $\beta$  are an empirical constant with  $\beta \in [0.3; 0.45]$  (respectively for rills and gullies, see Govers et al., 2000; Nearing et al., 1999). Using Equations (3), (12) and (11) we obtain Equation (10) with

$$k = \frac{W_{cr}}{\rho_f g k_u (R-I)^\beta} \quad (13)$$

Torri and Poesen (2014) developed an equation for predicting  $k$  values for GHs caused by rainfall excess runoff as a function of  $S_{0.05}$  (Hawkins et al., 2009). This parameter is a quantity derived from the Natural Resources Conservation Service (NRCS) CN method and representing storage and infiltration of rain. As discussed in Hawkins et al.'s (2009), it is linked to the original maximum potential storage and infiltration losses to runoff  $S_{0.20}$  by the following equation:

$$S_{0.05} = 0.819 S_{0.20}^{1.15} \quad (14)$$

where

$$S_{0.20} = 25.4 \left[ \frac{1000}{CN} - 10 \right] \quad (15)$$

with the  $S$  values expressed in millimetres (the constant 0.819 is measured in  $mm^{-0.15}$ ).

$S_{0.20}$  is derived directly from CN and it is a fundamental quantity in the NRCS method which appears in its basic equation for runoff ( $Q_{CN}$ , in millimetres) evaluation given the daily precipitation  $P$  (in millimetres) and the land use ( $S_{0.20}$ ):

$$Q_{CN} = \frac{(P - 0.20 S_{0.20})^2}{P + (1 - 0.20) S_{0.20}} \quad (16)$$

The equation for the threshold  $k$ , which was proposed by Torri and Poesen (2014), is the following:

$$k = 0.73 e^{1.3RFC} \psi [0.00124(S_{0.05} - 30)] \quad (17)$$

where  $\psi$  (originally named  $c$  in Torri and Poesen [2014]) represents all factors that may influence  $k$  but could only be identified for too a few cases to develop a possible correction factor (e.g., for GHs forming on joints or fault lines, or for the presence of piping at some depth). RFC is rock fragment content (estimated visually, hence it is a surface cover).

Unfortunately, Equation (17) predicts  $k = 0$  at  $S_{0.05} = 30$  which occur for relatively high CN values ( $CN > 90$ ) but values that are still possible ( $CN_{max} = 100$ ). Hence Torri, Poesen, et al. (2018) recalculated the relationship which brought to Equation (17) using a slightly different regression model (the new and old curves overlap for most of the range apart the values of  $CN < 35$ ), obtaining the following equation which predict  $k = 0$  for  $CN = 100$  and  $S_{0.05} = 0$ , where the RFC effects was recalculated:

$$k = RFC_{eff} \psi 0.00113 \left[ 1 - e^{(-0.0137S_{0.05})} \right] S_{0.05} \quad (18)$$

with  $RFC_{eff} = 0.4 [1 + e^{1.46RFC}]$

This mathematical summary shows that the CN method plays a relevant role, hence the method to estimate the CN value for a given land use needs a thorough definition. This article will also deal with a better defined procedure for calculating the CN value in badland and pre/post-badland environments, in order to reduce

the degree of arbitrariness in selecting CN values, even if we acknowledge that there will be room for future studies searching better methodologies.

## 1.2 | $\tan(\gamma)$ or $\sin(\gamma)$ : Additional theoretical basis for a new insight into the threshold model

Following the approach for the estimation of  $k$ , supported by Montgomery and Dietrich (1994) and expressed by Equations (9) and (10), the GH threshold depends on  $\tau_{cr}$  which is the threshold stress exerted by the flow on the soil particles and aggregates to entrain these. This critical stress is assumed to be proportional to the soil strength. A first model can be constructed assuming the forces expressed by vectors instead of tensors. The latter would require more basic data, which are usually not available, especially for such small soil depths (i.e., at the very surface) as discussed by Brunori et al. (1989). The resistance vector ( $\vec{R}$  expressed in pascals) of a soil grain per unit of soil surface may be expressed as follows. First, there is a component parallel to the slope ( $R_x$ ) due to the gravity component normal to the soil surface (pressure exerted over the surface of contact between the soil mass and the soil grain). This component must be decreased by the gravity component parallel to the soil surface (which is not included in the potentially detaching fluid stress):

$$R_x = (\rho_s - h_f \rho_f) g \zeta \cos \gamma \tan \varphi - (\rho_s - h_f \rho_f) g \zeta \sin \gamma \quad (19a)$$

where  $h_f$  (dimensionless) is the fraction of the grain (or rock fragment) that is actually submerged in the flow ( $h_f = 1$  represents total submersion) and  $\zeta$  (measured in metres) represents the diameter of the grain normal to the soil surface (usually the shortest grain or rock fragment axis),  $\varphi$  is the friction angle,  $\rho_s$  is the saturated soil grain density and  $\rho_f$  is the fluid density both expressed in  $\text{kg/m}^3$ .

Note that with increasing slope gradient the subtractive gravity component grows while the frictional part decreases, hence  $R_x$  necessarily decreases with slope.

The  $\vec{R}$  component ( $R_z$ ) normal to the soil surface is the component that is opposed to the runoff lift forces and equals:

$$R_z = (\rho_s - h_f \rho_f) g \zeta \cos \gamma \quad (19b)$$

The incipient motion of soil grains will occur in a certain direction following which of the two components of the drag/lift forces, produced by overland flow at the GH, dominates. Along this direction and opposite to the detaching force, another resistance force, due to various bonds between the grain and the surrounding soil grains, adds to  $\vec{R}$  and this is what is usually called cohesion ( $c$ ).

The only assumption made here for estimating the intensity of the resisting pressure, and then of the critical flow detaching force, is that of using the following estimation of the total resistance intensity, supposing that cohesion and  $\vec{R}$  have the same direction and sense:

$$|\vec{R}_{tot}| = |\vec{R} + \vec{c}| = \Delta \rho g \zeta \cos \gamma \sqrt{\{1 + (\tan \varphi - \tan \gamma)^2\}} + c \quad (20)$$

where  $\Delta \rho = (\rho_s - h_f \rho_f)$

Equation (20) is substantially a Rankine Coulomb approximation with a frictional and a cohesive component, the main difference being that it also contains the gravity detaching component.

As stated earlier, the critical fluid pressure (drag and lift) can be assumed to be proportional to the soil resisting forces per soil surface unit, that is  $\tau_{cr} \sim R_{tot}$ . Hence, the threshold equation can be rewritten to account for the additional dependence on  $\gamma$ . Let us now introduce Equation (20) into Equation (10):

$$\sin \gamma A^{0.4} > k \text{ with } k = \left[ \frac{k_w^{0.6} \left( \Delta \rho g \zeta \cos \gamma \sqrt{\{1 + (\tan \varphi - \tan \gamma)^2\}} + c \right)}{g \rho_f n^{0.6} (R - I)^{0.28}} \right]^{10} \quad (21)$$

The  $k$  value of Equation (21) corresponds to the  $k_{1st}$  part, a constant: we have substituted a fluid shear stress with soil resistance but, as Nearing (1991) noted, the fluid shear strength is much smaller than the soil resistance probably because only the most intense eddies could actually entrain the soil grains (hence, turbulent flow conditions).

Equation (21) introduces four new parameters to be estimated, that is cohesion, friction angle, average grain or rock fragment size, and submerged grain or rock fragment density. Some of these can be estimated from the literature, as shown later in the section. Now let us take a look at the theoretical threshold trends. The resistance term  $R_{tot}$  is made of two parts, only one changing with the slope angle  $\gamma$ . Hence, the threshold line will vary in shape between two extremes following whether the cohesion term is larger than the friction term or

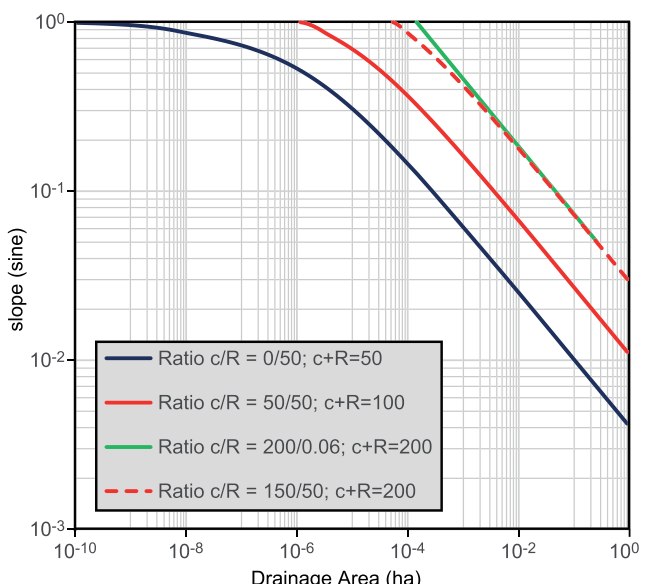


**FIGURE 1** Relation between hillslope gradient and drainage area at gully heads. Four curves are shown for four  $c/R$  ratios (0, 1, 3300, 3). The three ratios correspond to three total resistance values ( $c + R = 50, 100, 200 \text{ Pa}$ ). The third value (200 Pa) is obtained for two situations, one valid for a fine soil and one for a coarse soil but still rich in clay, hence with two different ratios of cohesive to frictional forces. The two corresponding curves differ only for steep gradient values. This bending is present in all the curves with a large frictional component (i.e., frictional component  $> 0.3$  cohesion) [Color figure can be viewed at [wileyonlinelibrary.com](http://wileyonlinelibrary.com)]

vice versa (Figure 1). If the cohesion term dominates over the frictional one (i.e., large values of  $c/R$  in Figure 1), the threshold line will be a straight line in the log-log area-slope plot (the hillslope gradient is expressed as the sine of the slope angle). Conversely if the frictional resistance becomes more and more relevant (i.e., low values of  $c/R$  in Figure 1), the threshold line will bend for low drainage area values. In such a case, the threshold straight line is obtained expressing the hillslope gradient as the tangent of the slope angle.

We can run some simulations varying the ratio between the vector intensities  $c/R$  from zero (only friction forces) to infinity (only cohesive forces) and see how the threshold curve varies.

The trends shown in Figure 1 indicates that one must expect a convex threshold line when the frictional component is sufficiently large, which is the case when  $R > 0.3c$ .

Let us now describe a way for estimating the frictional parameters. In order to estimate the friction angle, we can make use of some relationships reported by Poesen & Torri (1989) and Torri et al. (1990), in agreement with Nearing (1991). They found that for a grain or rock fragment of a given size and a given shape, its friction angle over a fixed bed is a function of the relative size of the grain with respect to the grain size of the bed. Re-examining their data and those reported in other studies (Biancalani, 1988, 1989; Dewilde, 1986; Torri & Poesen, 1988) it was possible to draw the trends shown in Figure 2, where the angular and the round rock fragment data were presented in Biancalani (1988), while the intermediate shaped rock fragment data are shown in Poesen & Torri (1989) and Torri et al. (1990).

These friction angles, as reported by Poesen and Torri (1989) and Torri et al. (1990), are distributed roughly following a gaussian

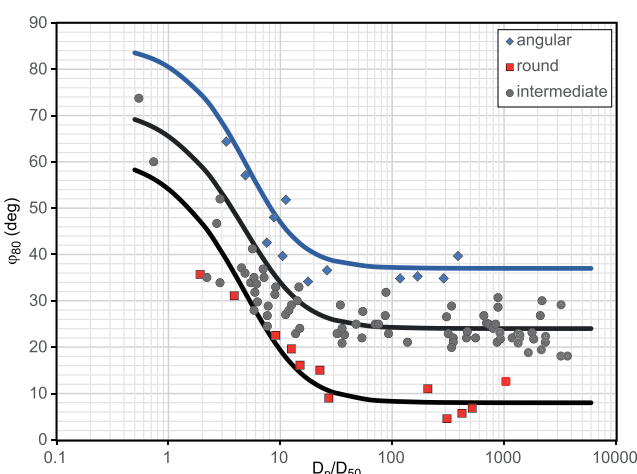


**FIGURE 2** The 80th percentile of the friction angle distribution ( $\varphi_{80}$ ) as a function of the relative rock fragment size ( $D_p$ , rock fragments) with respect to the median grain or rock fragment size ( $D_{50}$ ) of the channel bed. The friction angle  $\varphi_{80}$  expresses the probability of motion equal to 80%. The three curves show the effect of the rock fragment shape and roundness (angular means tending towards prismatic, with sharp corners, intermediates are more ellipsoidal in shape, while the round ones have bulging faces and rounded corners). The angular fragments are usually characterized by a ratio between the maximum ( $D_{max}$ ) and the minimum ( $D_{min}$ ) diameter larger than 2.5, the intermediate fragments have  $D_{max}/D_{min}$  ratios between 2.5 and 1, while for the round fragments this ratio varies between 1 and 1.3. [Color figure can be viewed at [wileyonlinelibrary.com](http://wileyonlinelibrary.com)]

distribution. As the friction angle does vary between  $0^\circ$  and  $90^\circ$  the equation of the gaussian curve should be modified for transforming the finite interval into an infinite one. As we are not looking for situations very close to  $0^\circ$  or to  $90^\circ$ , we will consider the usual form of the normal Gauss distribution.

Figure 3 represents the variation of the friction angle standard deviation for the same relative grain size as shown in Figure 1:

Combining the results shown in Figures 2 and 3, we can now calculate the mean value of the friction angles for soils, using the following formula:

$$\varphi_{50} = \varphi_{80} - 0.345 S_{d,\varphi} \quad (22)$$

where  $\varphi_{50}$  and  $\varphi_{80}$  are respectively the 50th and the 80th percentiles;  $S_{d,\varphi}$  is the standard deviation shown in Figure 3.

### 1.3 | The ratio between the fluid stresses and the soil resistance strengths

Usually one uses soil resistance characteristics which apparently do not match the stresses and pressures exerted by the fluid on the soil grains and aggregates to detach and entrain these. Actually, when one measures the soil resistance, whatever measuring device is used, the resulting resistance values are always larger than the fluid stresses measured using equations such as the one for the bottom shear stress. This is a problem that was addressed by Nearing (1991). Here, we follow this approach and add some means to evaluate the critical fluid stresses in the absence of any measurements of peak overland flow.

The following three statements summarize this and allow to further develop a model.

Nearing (1991) suggested that the distribution of fluid stresses for a given value of average fluid stress has a tail toward high stress values, that overlaps the tail of the distribution of soil grain resistances towards low soil strength values; this causes the apparent contradiction that lower fluid stresses erode soils with higher strengths (i.e., a low average fluid stress,  $\bar{F}_{stress}$ , will erode a soil with a much

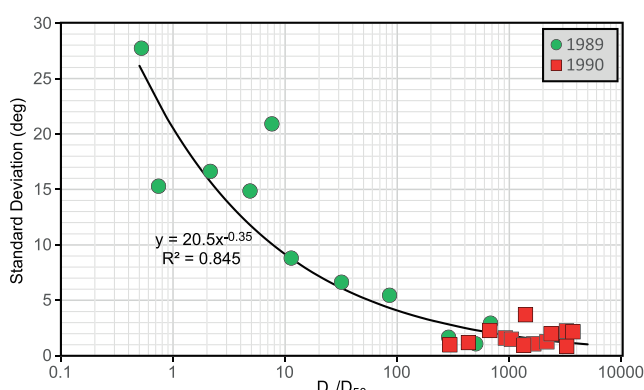


**FIGURE 3** Relation between the standard deviation of the soil grain friction angle ( $\varphi$ ) calculated from two data sets reported by Poesen and Torri (1989) and Torri et al. (1990) and the relative rock fragment size ( $D_p$ , rock fragments) with respect to the median grain or rock fragment size ( $D_{50}$ ) of the channel bed. [Color figure can be viewed at [wileyonlinelibrary.com](http://wileyonlinelibrary.com)]

higher average strength,  $\bar{R}_{soil}$ ); this is often represented through a ratio,  $FS_{ratio}$ , between  $\bar{F}_{stress}$  and  $\bar{R}_{soil}$ :

- i.  $FS_{ratio}$  resulted to be much lower than unity, with an order of magnitude given for rills by Torri et al. (1987) (corrected according to Brunori et al., 1989) and by Abdel-Rahman (1963) reported in Torri et al. (1987), having values of 0.0002 and 0.0004, respectively; those values can be considered as an approximate lower boundary value for gullies;
- ii. Smerdon and Beasley (1959, 1961) proposed an equation for evaluating the average critical fluid stress using the clay fraction (C) (see also Nachtergael et al., 2002):

$$\bar{F}_{stress} = \frac{1}{2} 10^{1.83C} \text{ expressed in pascals} \quad (23)$$

Note that when  $C=0$  then  $\bar{F}_{stress}=0.5$  Pa, independently from the shape and other variables driving the friction angle, as discussed previously (Figures 2 and 3).

Hence, we expect that the ratio  $FS_{ratio}$  between the fluid forces acting at the GHs and the soil resistance forces varies between  $0.0004 < FS_{ratio} < 1$ .

## 2 | GULLY HEAD DATA COLLECTION, MEASUREMENTS AND CHARACTERIZATION METHODS

### 2.1 | Study area description

Collection of GH data were made in different badland areas located in Italy and Spain, where GH processes contributed significantly to badland formation and evolution. Badlands developing in different sedimentary environments dominated by diversified lithological complexes were selected and studied to account for their heterogeneity and variability, namely (i) badlands developing in continental alluvial, predominantly gravelly sandy deposits (Guadalajara study area), (ii) badlands developing in marine silty clayey deposits (Leonina study area), and (iii) badlands developing in predominately marine marly thin layered deposits (Verghereto study area) (Figure 4). Within each study area, different sites were investigated to guarantee a proper sampling of the GH formation and development conditions in the different badland environments. Table 2 lists the location and characteristics of the GH study areas and measuring sites investigated in this study and reports the relative climate classification based on the updated Köppen–Geiger climate classification world map (Kottek et al., 2006).

The  $SO_{0.05}$  values are reported in the table according to US Department of Agriculture (USDA) NRCS CN method (USDA & NRCS, 2019). For the Hydrological Soil Group (HSG) identification, the depth of the first impervious layer and its hydraulic conductivity (estimated from texture using the ‘Soil Water Characteristics’ module of SPAW software developed by the Agricultural Research Service (ARS) USDA, see <http://irrigationtoolbox.com/NEH/UserGuides/SPAW%20User%20Guide.pdf> and Saxton et al. [1986]) were considered.

### 2.2 | Characteristics, origin and evolution of badlands

Verghereto and Montione badlands (Figure 4) share the same land-use history, given their proximity and the status of dependence of Montione with respect to Verghereto. The short description that follows is based on books such as Amati (1868), Rampoldi (1832), and Repetti (1841), more data can be found at the Emilia Romagna web site ([https://www.appenninoromagnolo.it/comuni/verghereto\\_storia.asp](https://www.appenninoromagnolo.it/comuni/verghereto_storia.asp), last visited 16 August 2021). Information of the badland history is based on a series of sources among which roman artefacts (more numerous near the town of Bagno with its thermal springs), middle age structures such as the St Peter church in Montione or the Verghereto castle, and the battles that brought this area under the sovereignty of the republic of Florence in the 1400. The area has always been described as wooded (beach trees, chestnuts) with important grasslands. The local wood industries sold its products largely to the Florentine territory until 1900. During the second half of the 19th century the wood market should have been more intense and livelier than usual thanks to the national rail road construction which reached 10,000 km by the beginning of the 20th century.

Grasslands were used as pasture for livestock to sell and for local animal farms. Livestock included cattle, sheep, and horses. Two, three fairs were usually organized each year during the 19th century. The same typology of land use still persists, even if sided by some tourism/holiday-linked activity (partly due to winter skiing on the nearby Mount Fumaiolo). Infrastructures such as a motorway or the distribution of the electricity network contributed to the local economy and to soil erosion. The morphology of part of the area had been defined as ‘dirupata’, that is ravine affected, sterile, and fragile, that is prone to erosion and mass movements, in most of the 1800 documentations, particularly near and around Verghereto. Contemporary documents with pictures show gullies and landslides in the entire territory with Verghereto standing over one of the locally greener areas. Present land use includes forest, part of them periodically cleared, cropland, forage grasslands, and meadow.

The soils can be distinguished in two typologies. Where erosion predominates the fractured rocks are covered by a thin layer (less than 10 cm) of finely fractured marly material. This layer consists of chaotically-arranged rock fragments, falling dominantly into the 0.5–5 cm diameter class), with very few herbaceous plants and mostly no organic layer. Where the soil is under a dense tree cover or grassland the following series were identified (Regione Emilia Romagna, 2021) such as Eutric Cambisols (WRB, 2015) under well-established forest even more than 1 m deep) while Calcaric Cambisols are found under cropland, grassland and meadow. Under newly established tree plantations the typical soils are Calcaric Regosols, 10 to 20 cm deep. Loamy-skeletal variations are also common.

Obviously, these soils characterize the area not affected by gully erosion. Where gully erosion dominates, the soils substantially consist of rock fragments, with a scarcely-developed soil horizon structure (A/C over C or directly over R with A/C horizon very shallow), particularly in Montione (Figure 4).

The Leonina badlands are located inside the protected Natura2000 area ‘Crete di Camposodo e Crete di Leonina’ (IT5190004), surrounded by croplands (Figure 4). Land-use history is

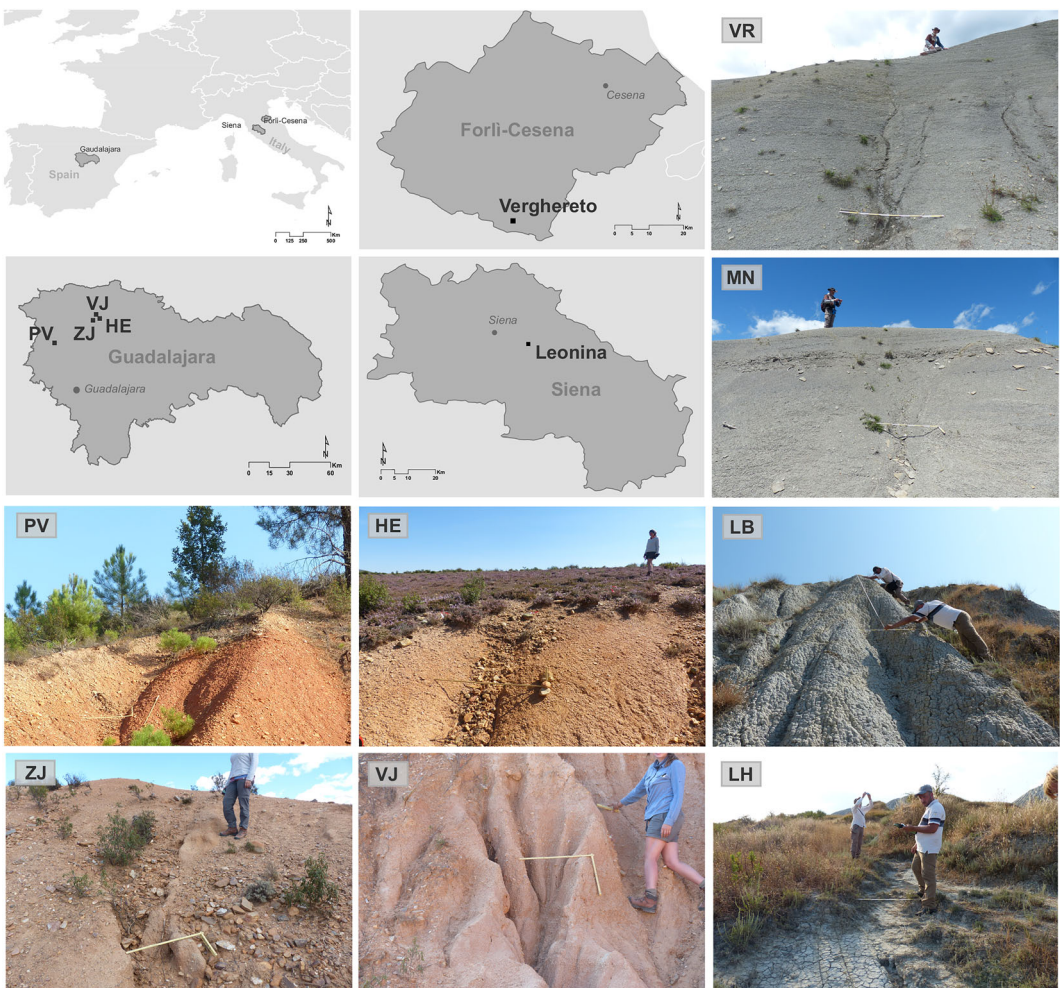


**FIGURE 4** Location of the badland study areas and illustration of the sampled badland sites. Site codes are reported in Table 2. [Color figure can be viewed at [wileyonlinelibrary.com](http://wileyonlinelibrary.com)]

**TABLE 2** Location and characteristics of the gully head study areas and measuring sites. Climate class is based on the updated Köppen–Geiger climate classification world map (Kottek et al., 2006)

Country	Study area	Site code	Location	Longitude	Latitude	Elevation	Number of gully heads	Köppen–Geiger climate classification	P (mm)	T (°C)	PET (mm)
									Grieser, 2006		
Spain	Guadalajara	PV	Puebla de Valles	-3.2921	40.9265	915	6	Csa	377	13.13	918
Spain	Guadalajara	HE	Hiendelaencina	-2.9982	41.0791	1098	6	Csa/Csb	377	13.13	918
Spain	Guadalajara	VJ	Villares de Jadraque	-3.0283	41.1098	1068	13	Csb	377	13.13	918
Spain	Guadalajara	ZJ	Zarzuela de Jadraque	-3.0512	41.0713	1062	33	Csa	377	13.13	918
Italy	Verghereto	VR	Verghereto	12.0442	43.7747	910	34	Cfb/Csa	740	12.44	752
Italy	Verghereto	MN	Montione	11.9881	43.7889	850	5	Cfb/Csa	740	12.44	752
Italy	Leonina	LH	Leonina Biancana	11.4474	43.2932	215	20	Csa	790	13.70	855
Italy	Leonina	LB	Leonina Hillslope	11.4474	43.2932	215	30	Csa	790	13.70	855

presented and discussed in Amici et al. (2017) and Torri, Poesen, et al. (2018), Torri, Rossi, et al. (2018). The suitability of croplands in this area has already been documented since AD 1000. Since 700–800 years ago, grazing (by sheep, goats, cattle, pigs) is also documented. This

most probably resulted in overgrazing (with periodical burning of the vegetation aiming at keeping the bush cover low) over the areas where the biancana badlands, like the Leonina ones, are documented. Particularly, the Leonina badlands first developed around

1300 (Torri, Rossi, et al., 2018), as deduced from biancana denudation rates determined by Chiaverini et al. (1999), most probably just after the first black death epidemic, which was reinforced by a series of plague upsurges during the following decades. This situation, which persisted for 50–70 years, kept the countryside poorly managed by lack of peasants and allowed soil erosion to expand and to transform a fertile territory into badlands. These biancana badlands are presently just a small remnant of what they were at the beginning of the 20th century. They were mostly transformed to cropland through a series of techniques of which the most effective was land levelling using bulldozers, which ended in the 1990s. The present land use (protection of the biancana geoform and the biodiversity it hosts) is such that vegetation has encroached the eroded slopes and the bare pediments for the last 20–30 years, substantially transforming most gullies into vegetated dormant gullies (Figure 4). Hence, the GHs are currently mostly inactive. Torri et al. (2013) showed that vegetation covers was much lower in the 1950s, when the bare biancana slopes were common (LB) and the interbiancana gullies (LH) had almost bare GH. Biancana badland remains are now located in the middle of croplands and invaded by grass and bushes, such as the ruderal species among which is the *Avena fatua* (Chiarucci et al., 1995; Maccherini et al., 2000). Plants such as *Artemesia cretacea*, *Hordeum maritimum*, *Parapholis incurva*, *Parapholis strigosa* and *Scorzonera laciniata* can be found where sedimentation prevails. At a more evolved stage with reduced sedimentation and erosion, *Aster linosyris*, *Bromus erectus*, *Dactylis hispanica*, *Phleum bertolonii*, and *Plantago lanceolata* are the grass dominant species (Chiarucci et al., 1995; Maccherini et al., 2000). Shrubs have recently expanded over an important fraction of the area, with covers ranging from 20% to 80%, especially on slopes and stable biancana domes. This vegetation is dominated by *Spartium junceum* and *Pyrus amygdaliformis*. Impluvia and foot slopes, where soil moisture is usually higher than elsewhere, hosts shrublands with *Spartium junceum*, *Pyrus amygdaliformis*, *Crataegus monogyna*, *Prunus spinosa* and sometimes *Ulmus minor*.

Soils consist of a patchwork of different types, which cannot be represented on a map unless at extremely large scales. Most studies describing the soils of these biancana badlands were conducted on similar badlands in the Orcia valley, c. 50 km southward (Calzolari, Ristori, Busoni, et al., 1993; Calzolari, Ristori, Sparvoli, et al., 1993). These soils range between Typic Xerorthents, fine, mixed (Calcareous), mesic and Calcixerollic (and Vertic) Xerochrepts, fine mixed (calcareous) mesic. Also, Chromic Haploixererts can be found on stable surfaces. Where the slope gradients are larger and where biancana domes dominate the soils are usually eroded entisols. In the better preserved spots, mainly on those biancanas which forms resemble irregular frustums, vertisols can be found, which can be relatively deep. Otherwise the biancana dome and slope soils are usually poorly developed with a A/AC-C profile. On active biancana pediments, where the horizon sequence is AC-C, the soils are silty-clay loam with a relatively silt-rich surface texture horizon due to the limited deposition of clay particles. Some of the best developed soils, with an almost complete sequence of horizons (A-AB-C; A-B-C) occur in morphological situations still preserving the soil developed before the events that resulted in the formation of the biancana badlands.

The Spanish badlands are located in an area where villages are very small with populations between 50 and 100 inhabitants (Figure 4), most

of which retirees (the younger population being present during weekends and vacation periods; De Geeter, 2018; Suárez, 2008).

The dominating plant species covering the study area are the evergreen shrubs *Cistus ladanifer*, which likes to grow on rocky soils, and *Rosmarinus officinalis*, more commonly known as rosemary. Both plants are native to the Mediterranean region and can resist drought and high temperatures as well as cold periods and take part of the typical matorral vegetation of the Mediterranean (Suárez, 2008; Ternan et al., 1996). In the 1960s, large parts of the region were reforested with pine tree species (e.g., *Pinus halepensis*, *Pinus pinea*) (Fitzjohn et al., 1998; Ternan et al., 1996).

According to the CORINE Land Cover classification of 2012 the land cover in the study area consists mainly of forest and semi-natural areas with at some places coniferous or mixed forest and at other places open or sparsely vegetated areas with shrubs (Figure 4). There is also some arable land, but it is scattered and mixed with natural vegetation (matorral). However, this has not always been the case. Traditional land use was often grazing, farming, and mining or local clay extractions (for pottery production). All these land-use types imply deforestation and exert important impacts on the landscape (Martín-Moreno et al., 2014).

The study sites are located in the Raña deposits (i.e., extensive piedmont alluvial deposits consisting of [weathered] siliceous clasts with fluvial sedimentological features). With these deposits being erodible, major soil erosion problems lead to extensive gullyling and even badland formation (Figure 4). There is not much known about land-use changes and human impacts for the study sites at Zarzuela de Jadraque, Villares de Jadraque and Hiendelaencina, but for Puebla de Valles some literature reports on the recent land-use history. For the other study sites, it can be assumed that the general situation is comparable to the one of Puebla de Valles. Until the 1940s the area around Puebla de Valles was intensively used for agriculture, which led to very degraded lands, the removal of the natural vegetation cover and to the erosion problems mentioned earlier (Suárez, 2008; Ternan et al., 1996). This situation was further reinforced due to the erodible soils and at some places extra land levelling was done to create large agricultural plots. Since the 1950s soil conservation measures were implemented, mainly reforestation projects as Puebla de Valles was part of the National Afforestation Plan that was implemented in Spain. In the 1970s a technique called bench-terracing developed which was used in the area of Puebla de Valles. Furthermore, check dams were installed in the largest active gullies. Despite these techniques not always being successful, the situation strongly improved: more than 50% of the area around Puebla de Valles is now covered by forest and there are several dams. Furthermore, the arable land area has strongly decreased as the present-day population of Puebla de Valles does not depend on agriculture to make a living. The reforested areas are now valuable for recreation, rural tourism, habitats for fauna and flora (Suárez, 2008).

The studied badlands are, which are still actively eroding, formed on the sidewalls of the erodible Raña plateau. A striking element in especially Zarzuela de Jadraque is the amphitheatrical shape of the badlands. It looks like the head scarp of a landslide but no sliding plain, reverse wall or depositional zone could be noticed. Such shapes were not yet observed in marl badlands, so it is interpreted as being related to the material properties.

Similar to land use and management, little information on the history of these badlands is available, but the studies of Ballesteros

Cánovas et al. (2017) and Martín-Moreno et al. (2014) tried to reconstruct the history of intensive gullying in sandy material in the same region. They suggested that the gully they studied probably started to form after deforestation begun in the 13th century and before the 18th century, when the gully was reported in historical documents. Their main conclusion is that badland formation mostly follows a period of deforestation and intense land pressure in combination with grazing and farming, as the main cause of gully and badland formation. The change of climatic conditions appears to be less important for the initiation of the gullies but could have played a role in its further development when more frequent and probably more intense freeze-thaw cycles caused further disintegration of the surface material during the Little Ice Age (Martín-Moreno et al., 2014). The land pressure decreased strongly from the second half of the 20th century onwards when the areas depopulated, traditional activities were abandoned

and reforestation was widely applied (Ballesteros Cánovas et al., 2017; Martín-Moreno et al., 2014; Ternan et al., 1996). However, after reforestation, as Ballesteros Cánovas et al. (2017) and Ternan et al. (1996) noticed, a phase of renewed channel incision occurred due to a concentration of runoff and thus erosion in the main gully channel because of a declined sediment connectivity between slope and gully channel (clear water effect). This indicates that the recent land-use changes are still affecting positively badland formation.

The resulting landscape is characterized by Eutric Cambisol soils (WRB, 2015). However, due to the strongly weathered character of the soils with disintegrated pebbles and clayey material, well developed soils can also be found and classified as Ultisols or Alfisols following Soil Taxonomy (Espejo Serrano, 1985; Gutierrez-Elorza et al., 2002). Badlands usually occur in the poorest soil situation.



**FIGURE 5** Instrumental settings used for the geometric and morphometric characterization of each selected gully head, in (a) the Leonina, (b) Verghereto, and (c) Guadalajara study areas. [Color figure can be viewed at [wileyonlinelibrary.com](http://wileyonlinelibrary.com)]

## 2.3 | Gully head selection

Within each badland site, the gully sampling locations were selected to guarantee the correct characterization and measuring of GH features. According to the definition of Hauge (1977), GHs with a cross-section perpendicular to flow direction larger or equal to about 1 ft<sup>2</sup> (i.e., approximately equal to 0.093 m<sup>2</sup>) were selected directly in the field. This criterion was adopted because it has been largely used in many studies for standardization purposes despite the fact that there are no physical reasons for this criterion (Poesen et al., 2003). Single and still active GHs selected were (i) the identification and measuring of the GH cross-sections was straightforward, (ii) the contributing area was easy to determine, (iii) the GH vegetation cover and land use was almost uniform in the contributing area; (iv) the human disturbances (e.g., roads, drainage systems, etc.) were absent in the contributing area and in the GH proximity. At each site, the collection procedure aimed at maximizing the range of GH slope gradients and contributing areas selecting among those where the drainage area and slope gradient around the GH were more clearly detectable.

## 2.4 | Field-based gully head characterization

For each selected GH, several field observations and measurements were made. Samples of soil/regolith in the top 10 cm nearby the GHs were collected for textural analysis.

Morphological characteristics of each GH were measured using different instrumental settings according to the different badland environments, to the accessibility of the GH and to the contributing area dimensions. Specifically, the gully channel perimeter, width, depth and cross-sectional area were determined at the GH, where local soil surface slope and contributing area were also measured. The three instrumental settings were (Figure 5):

- i. Leica Zeno 15 GNSS/GIS handhelds with RTK correction with decimetric accuracy (maximum horizontal and vertical accuracy > 20 cm), manual stick and tape meters and a digital inclinometer;
- ii. Leica Zeno 15 GNSS/GIS handhelds with RTK correction with decimetric accuracy (maximum horizontal and vertical accuracy > 20 cm) and Leica DISTO™ S910 Pro Pack 3D laser distance measurer with millimetric accuracy;
- iii. Leica Zeno 20 GNSS/GIS android handhelds with RTK correction with centimetric accuracy (maximum horizontal and vertical accuracy > 1 cm) and Leica DISTO™ S910 Pro Pack 3D laser distance measurer with millimetric accuracy.

While instrumental settings (i) allow measurement where GHs are directly accessible, the settings (ii) and (iii) allow remote measurements with different accuracies. Such remote measurement capability relies mostly on the ability of the Leica DISTO™ S910 (combined with Leica FTA360-S tripod micrometric adapter and Leica TRI 70 tripod) to measure vertical and horizontal angular distances to the target in addition to the line of sight (LOS) distances. These three observations allow the Leica DISTO™ S910 to calculate for a remote target automatically linear distances (e.g., segment lengths, object perimeters, etc.), surfaces dimension and slope angles. For the settings (ii) and (iii), the Leica DISTO™ S910 can be combined manually with Leica Zeno

15 GNSS/GIS handhelds or automatically with Leica Zeno 20 GNSS/GIS handhelds, to get a TPS-similar setup allowing the georeferentiation of the inaccessible or unreachable targets from a safe distance and to collect data in areas even where the GNSS reception is poor. The instrumental setting (i) was mostly used in Italy in the Leonina study area, the setting (ii) in the Verghereto study area, and the setting (iii) in the Guadalajara (Spain) study area (Figure 5).

Besides the geometric and morphometric gully characterization, additional field observations were taken for each GH. In the corresponding catchment area, the vegetation cover and the rock fragment cover were visually estimated. In addition, the rock fragment content was estimated at the critical gully cross-sections. Near some representative GHs, samples of soil/regolith of approximately 1 kg were taken in the first 10 cm of soil to measure the rock fragment content by mass afterwards. Such determination was done through manual sieving in the field using a 2 mm sieve, or later determined in the laboratory using an automatic sieve shaker. Ranges of RFC by mass for the different sites are reported in Table 3. The comparison RFC by mass (after sieving) with the visually estimated RFC in the field allowed to evaluate the reliability of field estimations.

Table 3 also provides information on lithology, HSG identification (USDA & NRCS, 2019), land use and cover in the past and in the current conditions, with the estimation of the vegetation cover during GH formation. Such characterization was made based on the historical information collected for the different locations.

## 2.5 | Gully head threshold value and Curve Number parameterization criteria

In this section, the criteria applied for the determination of both  $k$  and  $S_{0.05}$  are described. The former will be always calculated as the first percentile ( $k_{1st}$ ) of the observed distribution of the  $k$ -values calculated as  $k = \sin(\gamma)A^{0.4}$ , with  $\gamma$  and  $A$  being measured for a set of GHs in the field. The latter, that is  $S_{0.05}$ , will be selected considering that the resistance of the land-use soil system can change during the year, following seasons or generally following time and the many causes of modifications such as plants growth, symbiotic behaviour (e.g., mycorrhiza), soil biomass modification, anthropic direct interventions (e.g., tillage), grazing, changes in grazing management, to mention just a few of what is an almost never ending list of sources. The situations corresponding to the conditions for maximum hazard of GH retreat will be selected, for example, usually keeping the possible choices within the range of vegetation cover below 0.3 as this value brings soil resistance already pretty high thanks to the herbaceous root effect (De Baets et al., 2008; Thornes, 1985; Torri, Rossi, et al., 2018). Presence of cropland will bring in the seed bed situation. Usually, potential crop field that are difficult to protect from erosion damages are abandoned and land use shift to poor pasture or to rangeland, with frequent episodes of overgrazing, hence rangeland in poor to medium soil hydraulic conditions.

The  $S_{0.05}$  is then calculated through Equations (14) and (15) once a CN value is selected. The main reference guide to CN value identification remains the CN tables (USDA & NRCS, 2019), but other sources could be used when available (Descheemaeker et al., 2008). Preference will be given to the presence of relationships between CN and vegetation cover or vegetation biomass with respect to table

**TABLE 3** Characteristics of the selected gully head measuring sites (for site codes see Table 2): Lithology, land use and vegetation cover, soil texture, hydrological soil group (HSG, from USDA & NRCS, 2019) and rock fragment content (RFC) by mass in the topsoil

Site code	Lithology	Land use during gully head formation	Current mean vegetation cover (vegetation cover during gully head activity) (%)	RFC by mass (%)		
				HSG	Minimum	Maximum
PV	Alluvial deposits of siliceous conglomerates composed of a matrix of sands or red clays with a significant gravel fraction and rock fragments up to 30 cm diameter. Gravels (mostly shales and/or quartzites but showing local differences) are rounded and ellipsoidal and deposited in different orientations (e.g., showing imbrication structures) <sup>a</sup> .	Bushland and trees with grazing, farming and mining (mostly bare contributing area)	1.6	Silt loam (Loam)	D	59
HE	Similar to PV but with less gravel consisting of a mixture of (partly) rounded and angular gravel and with a matrix less red consisting of more sandy material as a result of the weathering of quartzites <sup>a</sup> .	Bushland with grazing, farming and mining (mostly vegetated contributing area)	50	Sandy clay loam (Clay)	D/C	9
VJ		Bushland with grazing, farming and mining (mostly bare contributing area)	3.4	Sandy loam	D	17
ZJ		Bushland with grazing, farming and mining (mostly bare contributing area)	5.9	Sandy loam (Sandy clay loam)	D/C	14
VR	Regular alternations of sandstone and predominant pelitic marls (i.e., siltstone and mudstone) <sup>b</sup> .	Forest and pasture (mostly bare contributing area)	3	Sand (Loamy sand)	D	68
MN		Forest and pasture (mostly bare contributing area)	3	Sand (Loamy sand)	D	90
LH	Plio-Pleistocene marine silty clay or clayey silt texture (USDA classification) rich in salt, particularly sodium with dispersive characteristics <sup>c</sup> .	During gully head formation: rangeland (sparsely vegetated and grazed contributing area). At present: protected land (vegetated contributing area)	86 (15)	Silty clay	D	0
LB		Rangeland (bare contributing area) At present protected land	13 (2)	Silty clay	D	0

<sup>a</sup>Summarized from Atienza and Pascua (2005), Espejo Serrano (1985), Molina Ballesteros and Cantano Martín (2002), Saldaña et al. (2011) and Suárez (2008).

<sup>b</sup>Deduced from Milighetti et al. (2009).

<sup>c</sup>Deduced from Torri et al. (2013), Torri, Poesen, et al. (2018), Torri, Rossi, et al. (2018).

averages. The vegetation/land use situation will be selected following the average CN value calculated over the range of possible values determined on the basis of the earlier considerations. The equations we used to estimate CN from land-use and vegetation cover are presented in the following lines.

Descheemaeker et al. (2008) published Ethiopian data relating vegetation cover to CN and they found that CN values for grazing land and no-grazed rangeland (enclosures of different age) is described by both the following relationship, where  $V_c$  is vegetation cover (fraction):

$$CN = 100 - 8.99 e^{2.1 V_c} \quad (\text{fA1a})$$

and

$$CN = 116 - 81V_c \quad (\text{fA1b})$$

with the mean value of CN for grazing land and for ARC=II corresponding to 95 (ARC is antecedent rainfall condition, the old AMC, with M for moisture and II refers to the second/middle class of ARC as reported in USDA & NRCS (2019)).

The problem with Equations (fA1a) and (fA1b) is that the former underestimates the CN for low cover values, while the latter gives very high CN estimate for  $V_c < 0.2$ , hence we will always use the mean value of the two trends.

From Branson et al. (1981) on herbaceous vegetation, we get the following equation

$$CN = 95 - 11.5 V_c \quad (\text{fA1c})$$

Meanwhile, interpolating over bare fallow, pasture, and grassland from the official runoff curve number table (USDA & NRCS, 2019), we get:

$$CN = 93.6 - 15.6 V_c \quad (\text{fA1d})$$

Still from Branson et al. (1981), we have

$$CN = 93 - 6 V_c \quad \text{for desert brush} \quad (\text{fA1e})$$

$$CN = 91 - 13 V_c \quad \text{for pasture, rangelands and annual grass} \quad (\text{fA1f})$$

$$CN = 87 - 21 V_c \quad \text{for forest} \quad (\text{fA1g})$$

From Romero et al. (2007), Taguas et al. (2015) and further crop cover descriptions by Meerkerk et al. (2008):

$$CN = 94 - 34 V_c \quad \text{for olive grove/almond grove} \quad (\text{fA1h})$$

As an example, for a vegetation cover  $V_c = 0.05$ , for a land use corresponding to almond grove, abandoned fields, brush cover; climate semi-arid, with gullies developed mainly on almond grove and secondarily in abandoned fields, the CN should be something in between almond grove and abandoned fields. With a low vegetation cover we can use Equation (fA1d) for calculating CN for the abandoned land, and Equation (fA1h) for almond grove. The average of the two CN (or the weighted average when data allow) will then be used for calculating the  $S_{0.05}$  value. In case active gullies were observed also

under the brush cover, for instance characterized by a different vegetation cover, for example,  $V_c = 0.15$ , then a third CN value should have been calculated with Equation (fA1e) and the resulting CN calculated as the average of the three values (either as an arithmetical average, or weighing each CN by the fraction of GHs attributed to each use).

This method reduces arbitrariness once the land-use type and cover values are identified and quantified. Having the researchers aware that being wrong or scarcely defined in the evaluation of the earlier listed quantitative characteristics does reduce the certainty of correctly evaluating thresholds, then they will be more careful in their observations (lack of information on vegetation cover or on rock fragment cover was the base for the reducing to a quarter the total number of GH field data in the review paper by Torri and Poesen (2014)).

### 3 | RESULTS AND DISCUSSION

This section summarizes and discusses the results of the analysis performed to characterize the climatic conditions at the different GH sites and the results of the field measurements and observations at each GH.

Average monthly climatic statistics obtained for the different sites from the daily E-OBS gridded dataset at 0.25 degree of resolution are shown in Figure 6. The sites LB and LH being close in space, resulted in the same grid cells and hence described by the same values. The sites ZJ, VJ and HE showing minor differences in terms of monthly average statistics were grouped. All sites reveal a classical Mediterranean precipitation pattern with two peaks in fall and spring with a 6 months distance (Figure 6b), and a hot dry summer with the Spanish sites always the driest. The air temperatures do not separate clearly the climatic conditions of the study sites, particularly considering the maximum air temperature ( $T_{\max}$  Figure 6b). LB, LH and PV show similar monthly  $T_{\max}$  distributions, with ZJ, VJ and HE being the coolest of all sites and LB and LH the warmest. This points to a potentially higher rate of material weathering in the Italian sites, with more rain, larger air temperature excursions both monthly and during the year.

Table 4 report values of different climatic indices complementing the average monthly climatic characterization. Such values were calculated starting from daily mean, minimum and maximum air temperature and precipitation data from the E-OBS dataset. The full index description can be found in Table 1. In Table 4 the sites ZJ, VJ and HE are shown separately to illustrate the differences characterizing the Spanish sites. In Table 4, SU and TN/TR indexes mainly characterize the summer period and describe respectively the day and night temperature condition. Rarely temperature conditions in the night reach extreme values, with only VR having more than one tropical night. During the day, temperature conditions can be different among the test sites, with VR and MN having the lower number of summer days (SU) probably due to the higher altitude. LB, LH and PV for almost the entire summer period and in September, show extreme day temperature conditions, with the larger day/night excursions. VR ad MN are the wettest sites with the higher average cumulative annual and seasonal precipitations (i.e., higher value of PRCPTOT, PRCPTOT\_DJF, PRCPTOT\_MAM, PRCPTOT\_JJA, PRCPTOT SON, PRCPTOTX\_SEASON, R95pTOT, R99pTOT) and with the higher number of days with rain (i.e., higher R10 and RR1 values). Conversely, the Spanish sites ZJ, VJ, HE and PV show the driest climatic conditions. As highlighted by the higher values

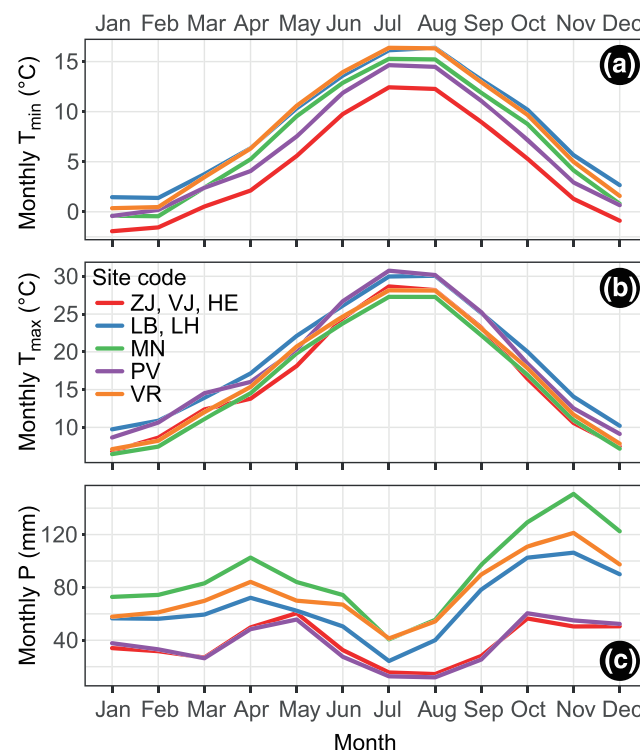


**FIGURE 6** Comparison of minimum (a) and maximum (b) air temperature and precipitation (c) monthly average statistics calculated for each gully head site (see Table 2). [Color figure can be viewed at [wileyonlinelibrary.com](http://wileyonlinelibrary.com)]

of the rainfall concentration indexes RX1DAY and RDN, the more intense precipitations are expected in the Italian sites (LB, LH, VR and MN). As shown by SDRR, snow is rare in the Leonina study area (LB and LH), while it may occur for a few days in a year in the other study areas and particularly in ZJ, VJ, VR and MN sites. The aridity indexes AIDM, AIDM\_MM and AP, counterintuitively to their names, show arid conditions when indexes values are low. The analysis of such values reveals the more arid conditions in the Guadalajara study area (ZJ, VJ, HE and PV sites) and the less arid in the Verghereto study area (VR and MN sites).

Field measurements and observations of the selected GHs allowed to diversify GHs based on different characteristics. Box plots in Figure 7 describe and compare the observed variability of the main morphometric, geometric and environmental characteristics of the GHs analysed in the study sites. The larger values of the gully catchment areas (Figure 7a) are observed at the Leonina (LH, hillslope) and in the Hiendelaencina sites where vegetation cover is larger (Figure 7b). This reflects the smaller runoff volume per unit of area generated in such conditions, requiring larger areas to produce the overland flow discharge needed to initiate a gully. The slope values measured at the GHs are highly variable in most sites (Figure 7c), with the smallest variability observed in the Hiendelaencina and in the Montione sites characterized by flat hillslope surfaces with almost uniform slope gradients. The cross-section of the GHs measured in the field (Figure 7e) are slightly larger and variable than the critical value of  $1 \text{ ft}^2$  ( $0.0929 \text{ m}^2$ ) used in other studies to define a gully (Poesen et al., 2003). This is related to the difficulty to select a proper gully cross-section in the field, which may vary significantly along the gully channel even over a short distance. However, these small variations

corresponding in general to shifts of the gully cross-section measurement locations along the channel of few centimetres, do not correspond to significant changes in GH catchment area and soil surface slope values. The slightly larger variation of the GH cross-section perimeter and average depth (Figure 7f,g) reflects the complexity and the roughness of the gully channels, which is particularly larger in badland environments.

The RFC by mass is highly variable in the different sites (Figure 7d). The values of RFC by mass determined by sieving and the corresponding values estimated visually in the field are shown in Figure 8. The comparison of RFC by mass values corresponding to fragment diameters larger than 2 mm are shown in Figure 8(a), while Figure 8(b) compares different RFC by mass determinations for the Verghereto study area, done in the laboratory from a full fragment-size distribution obtained using an automatic sieve shaker. In Figure 8(b) the mass corresponding to fragments diameters larger than 2, 4 and 6.3 mm are shown. Figure 8(c) shows the average values of RFC estimated visually in the field and their corresponding RFC by mass determination for particles fragments larger than 2 mm. This reflects the fact that RFC by mass was determined only at representative locations, hence each sieved sample corresponds to several visual estimations. The correspondence between RFC visual estimated in the field and the RFC by mass values determined by sieving, were evaluated through linear fitting and the relative results are summarized in Table 5. For each subset, Table 5 reports the sample size, the fitting coefficients and their significance as well as the  $R^2$  and its significance.

Differences between the RFC by mass values and the values visually estimated in the field are expected, since the latter is necessarily biased when the distance between the observer and the soil surface is larger than c. 50 cm and additionally conditioned by the observer eyesight quality and by visual defects. In addition, another possible explanation of such differences is related to the fact that the RFC by mass determinations, in some sampling conditions, may account not only the RFC at the soil surface but also incorporates subsurface fragments. Indeed, in general the number of RFC at the soil surface is larger than below the surface, because of erosion pavement formation. Obviously, the rock fragment cover is estimated with a surface as unit reference while the by mass content is automatically referring to a volume (or better to a mass of soil, always three dimensional). However, in the study areas the sampling for RFC by mass determination was done collecting material from the first 10 cm of topsoil, hence being representative for the surface and topsoil condition. The  $R^2$  results in Table 4 reveal that visual estimation better relates to RFC diameters larger than 4 mm. The correlation improves when the visual estimations are averaged over all those corresponding to the same by mass sample. In particular, for the average values the angular coefficient is the closest to one and the intercept to zero indicating a better degree of correlation. We acknowledge that the RFC determinations either measured by sieving or visually estimated in the field, are rarely described in detail in the literature. This may potentially introduce biases in the analyses. We therefore suggest to use the more objective RFC by mass values specifying the sampling depth and the sampling and measuring conditions.

The soil surface slope and catchment area values measured in the field of the different badland study areas are shown in Figure 9(a). In

TABLE 4 Values of the climatic indexes calculated for each gully head site in the study areas (see Table 2)

Climate index						
Site code	SU <sup>a</sup>	TN/TR	R10 <sup>a</sup>	PRCPTOT <sup>a</sup>	PRCPTOT_DJF	PRCPTOT_MAM
ZJ_VJ	81	0	12	514	139	154
HE	93	0	9	448	115	136
PV	101	0	12	441	122	129
LB, LH	103	1	28	794	202	193
VR	79	4	30	917	214	222
MN	69	1	39	1080	268	268

<sup>a</sup>Indicates the subset of indexes used for the optimal climate clusters classification.

TABLE 4 (Continued)

Climate index						
Site code	PRCPTOTX_SEASON	PRCPTOTX_SEASON_MONTHS	RX1DAY <sup>a</sup>	RR1	SDDR	R95pTOT
ZJ_VJ	189	OND	43	84	9	228
HE	159	OND	36	78	5	206
PV	170	OND	45	73	4	230
LB, LH	295	OND	82	91	0	405
VR	332	OND	66	114	8	401
MN	404	OND	67	116	9	455

<sup>a</sup>Indicates the subset of indexes used for the optimal climate clusters classification.

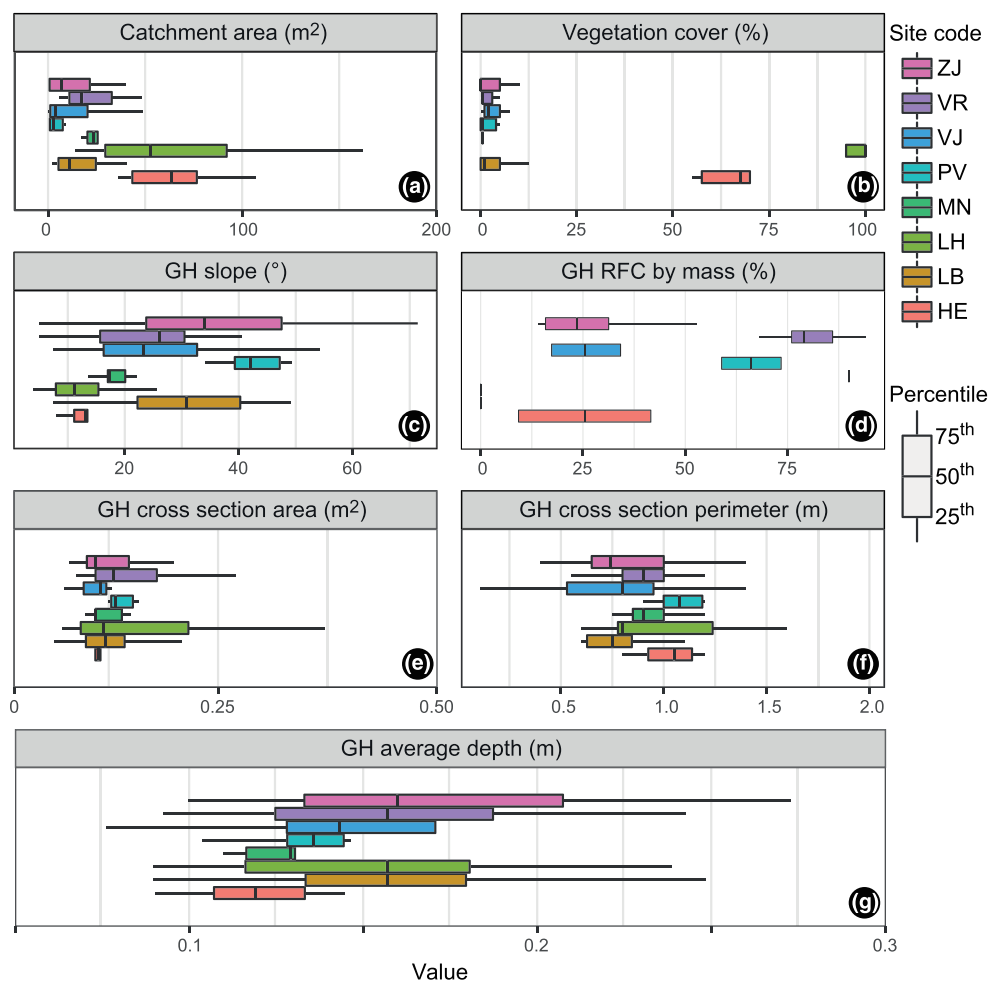


**FIGURE 7** Variability of gully catchment (a, b) characteristics and gully head (GH) geometric and morphometric features (c, d, e, f, g) within different GH sites (see Table 2). [Color figure can be viewed at [wileyonlinelibrary.com](http://wileyonlinelibrary.com)]

Figure 9(a), solid and dashed coloured lines show, respectively, the median and average threshold trends determined for cropland (red), rangeland (purple), and forest (green) (Torri & Poesen, 2014). The lower positions of the median trends imply asymmetric distributions of the  $k$ -values used for determining the different threshold trends. With respect to the other main land-use classes, the badland data plot lower, corresponding to a larger erodibility. The partial overlap of the badlands data with the cropland confirms that tillage is a powerful mean to undermine the soil and land-use system resistance to gully erosion. Also rangeland is partially overlapping the badlands (the median line plots already below two badland GH points, suggesting that the lower 50% of the rangeland observations are mixed with the badland ones), which suggest that badlands can develop directly from this land use. The variability of  $k$  values (Equation 10) is shown for the different study sites (Figure 9b) and for the different study areas (Figure 9c). The tangent of the slope is used rather than the sine value to better represent the  $k$  value variability for high slope gradients. Table 6 summarizes the percentile statistics of  $k$ -values estimated for the different study sites and study areas. GH morphometric characteristics in the different study areas are partially overlapping and in continuity among each other. The lowest median  $k$ -values can be observed in the two Spanish study sites VJ and ZJ and the highest in VR (Figure 9b). The lower boundary  $k$ -values (i.e., the most probable estimators of the threshold) seem to vary within a small range over the different areas (Figure 9c).

### 3.1 | The grain size distribution and the soil resistance to detachment

In Figure 9(a) the tangent instead of the sine was used for representing the effects of slope angle ( $\gamma$ ) on GH thresholds. This is not the expected trend (i.e., sine  $\gamma$  versus area) which results from the dependence of the flow characteristics (shear stress) on the sine of the slope angle. Figure 9(a) shows that the trend for the Spanish data are rectilinear if the gradient is expressed as a tangent instead of a sine. According to what is presented earlier the friction angle component seems to dominate. Hence, one needs to compare the field data and trends with evaluations of the two components which depend on the effective friction angle (Equation 21).

There are different elements to be considered for such evaluations. The first is the particle diameter representative for the eroded soil. This must be calculated using the grain size distribution extended to include the RFC by mass sampled in the top 5–10 cm of soil. As representative diameter, we use  $D_{50}$ , hence the ratio  $D_p/D_{50} = 1$ . This can be calculated for all our sites. Each site will be represented by the median grain diameter averaged over all the samples.

A second element to consider is the average bulk density, which depends on the soil characteristics: if the soil is aggregated, the bulk density (at saturation) is a reasonable value, if it is dispersed/flocculated because of the presence of high sodium content, the values of density may be much lower than for an undispersed clay. If the soil is fresh of

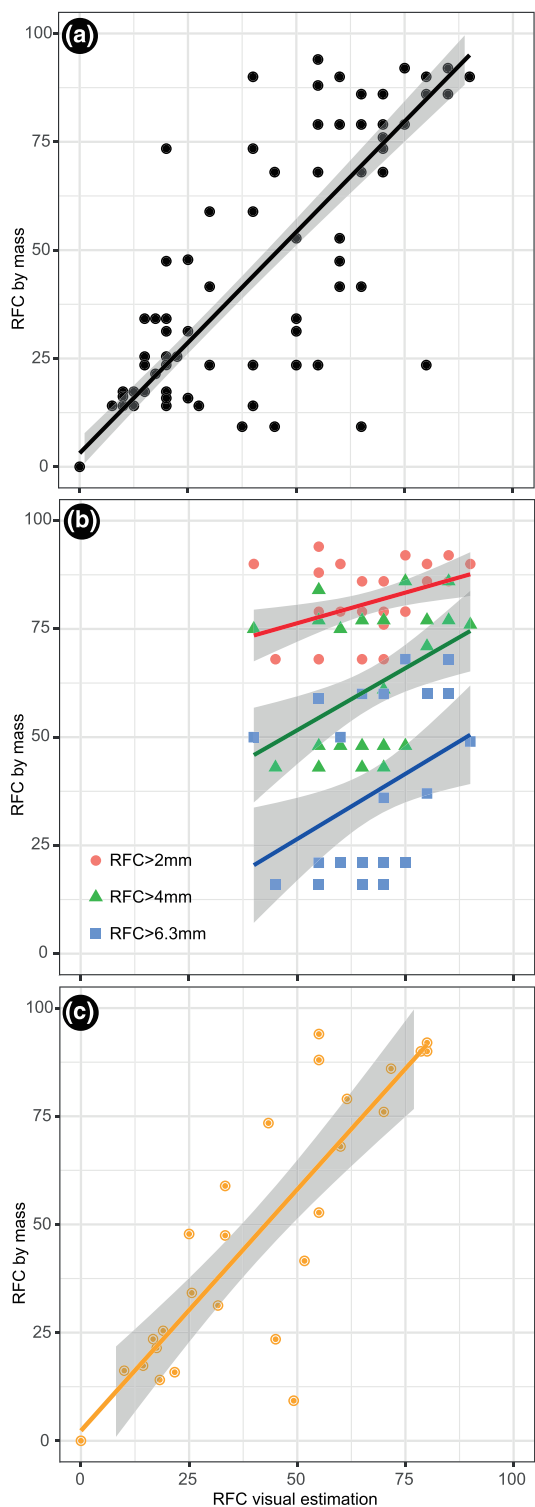


**FIGURE 8** Comparison of rock fragment content (RFC) by mass determined by sieving and the corresponding value estimated visually in the field. (a) RFC by mass values with fragment diameters larger than 2 mm in the Guadalajara and Verghereto study areas. (b) RFC by mass values with fragment diameters larger than 2, 4 and 6.3 mm in the Verghereto study area. (c) Average values of RFC estimated visually in the field in the Guadalajara and Verghereto study areas and corresponding RFC by mass determinations (done by sieving only for representative locations) for fragment diameters larger than 2 mm. [Color figure can be viewed at [wileyonlinelibrary.com](http://wileyonlinelibrary.com)]

weathering, its density will be very close to the density of the unaltered rock. The more the weathering the lower the density of the grains. Values can be found in Poesen and Lavee (1994).

To evaluate the position of the threshold curves for the different study sites, we adopted the values of the parameters reported in Table 7, where the values of cohesion were used for obtaining a perfect match between the  $k_{1st}$  value and the one calculated with Equation (21).

Results are shown in Figure 10. Regarding the LH and LB sites, the friction component was absolutely negligible and the position and shape of the threshold curve was defined only by the cohesion value. Note that Torri et al. (2013), Torri, Rossi, et al. (2018) evaluated the cohesion value of the saturated material to be below 500 Pa due to the dispersive action of the exchangeable sodium. The material was transported as floccules due to the high salt concentration in the runoff (2550–5000  $\mu\text{S}/\text{cm}$ ) hence the low values for the  $\Delta\rho$  in Table 7.

The relationship between the measured  $k_{1st}$  and  $R_{tot}$  (i.e., the average soil resistance over the observed surface gradient range, calculated with Equation (20) and data in Table 7) is obtained using Equation (21) for all the eight study sites:

$$k_{1st} = 0.000015 R_{tot}^{10/7} \quad (24)$$

where the constant 0.000015 is evaluated as the linear best fitting coefficient between  $k_{1st}$  and  $R_{tot}^{10/7}$  assuming a nil intercept. In other terms,

$$\left( \frac{k_w^{0.6}}{g\rho_f n^{0.6} (R - I)^{0.28}} \right)^{10/7} \approx 0.000015 \quad (24a)$$

from which it follows that:

$$k_w = 0.000002353 n (g\rho_f)^{5/3} (R - I)^{7/15} \quad (24b)$$

Equation (24b) offers the opportunity of evaluating this theory through a careful study of tributary junctions (Torri et al., 2006, 2012).

As discussed in Section 1.3, we expect that the ratio between critical fluid stresses and soil resistance values ( $FS_{ratio}$ ) should be included in the interval 0.0004 and 1. The estimated soil resistance  $R_{tot}$  is not the average soil resistance, as it would have been measured using a torvane or other device, but this is rather an estimation of the resistance offered by the grains that can be detached and entrained by the flow, and hence it is smaller than the average soil resistance  $\bar{R}_{soil}$ . Consequently, we expect a  $FS_{ratio}$  much larger than 0.0004.

If we estimate the critical fluid stress ( $\bar{F}_{stress}$ ) values using the Smerdon and Beasley (1961) formula (Equation 24), we can use these to calculate  $FS_{ratio}$ . The average  $FS_{ratio}$  for the eight badlands sites gives

$$FS_{ratio} = 0.013 \pm 0.012$$

If we average the  $FS_{ratio}$  of the non-dispersive soil (i.e., excluding the LH and LB sites), then the average ratio becomes:

$$FS_{ratio} = 0.0067 \pm 0.0022$$

In both cases the  $FS_{ratio}$  values fall well within the predicted range.

Such value is indeed larger than 0.0004 (lower boundary value estimated for rills), but is still quite below 1. Hence,  $\bar{F}_{stress}$  and  $R_{tot}$

**TABLE 5** Linear fitting results comparing rock fragment content (RFC) by mass values with RFC estimated visually in the field (see Figure 8)

Study area	Sample size	Sieve	Angular coefficient	Intercept	R <sup>2</sup>	Significance
All (Figure 8a)	95	> 2 mm	0.32	20.4	0.117	+++++
Verghereto (Figure 8b, red)	37	> 2 mm	0.28	62.2	0.192	+++
Verghereto (Figure 8b, green)	37	> 4 mm	0.57	22.9	0.226	++++
Verghereto (Figure 8b, blue)	37	> 6.3 mm	0.60	-3.9	0.178	+++
Averages (Figure 8c)	28	> 2 mm	1.12	2.3	0.737	+++++

Note: in the table the following significance codes were used: '+++++' [0,0.001] - '+++' [0.001,0.01] - '++' [0.01,0.05] - '+' [0.05,0.1] - '+' [0.1,1].

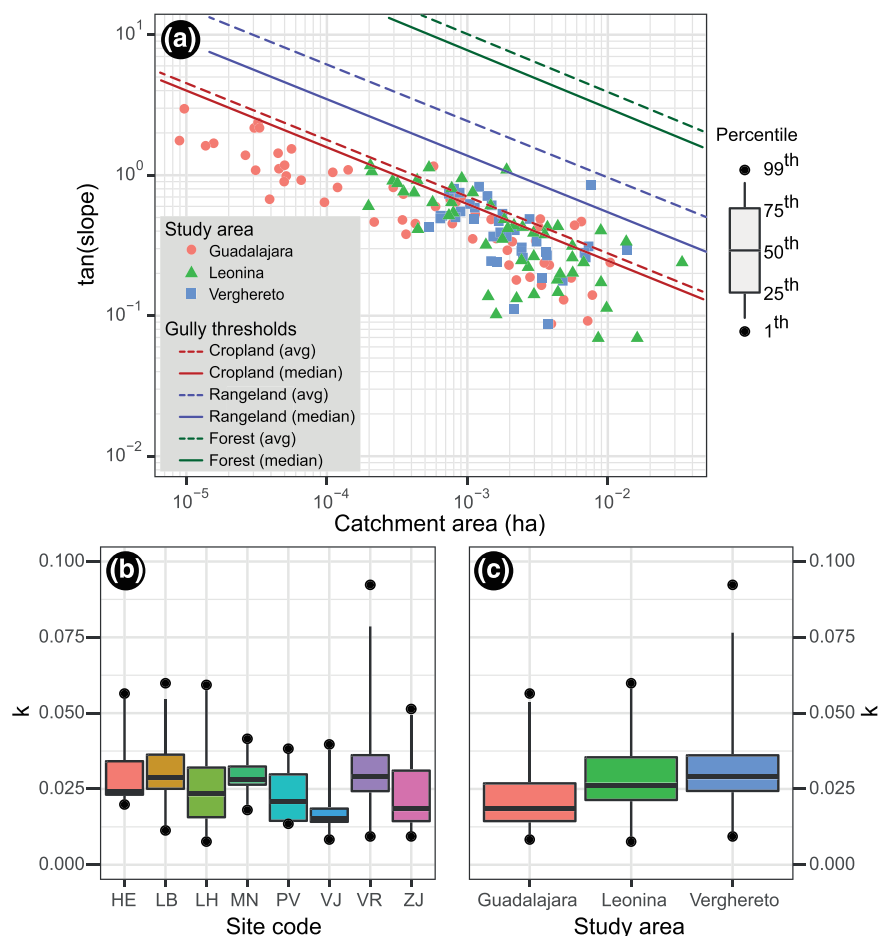


**FIGURE 9** (a) Soil surface slopes ( $\tan \theta$ ) at the gully heads and their corresponding catchment areas (a) measured in the different badland study areas (see Table 2); solid and dashed coloured lines show, respectively, the median and average threshold trends determined for cropland (dark red), rangeland (purple), and forest (green) (Torri & Poesen, 2014). Variability of  $k$  values (Equation 10) for the different badland study sites (b) and study areas (c). [Color figure can be viewed at [wileyonlinelibrary.com](http://wileyonlinelibrary.com)]

**TABLE 6** Percentile statistics of  $k$  values (Equation 10) calculated for each study site and for each study area (see Table 2)

Site code/study area	Percentile								
	Minimum	1st	5th	25th	50th	75th	95th	99th	Maximum
HE	0.020	0.020	0.021	0.023	0.024	0.034	0.052	0.056	0.056
LB	0.011	0.013	0.017	0.025	0.029	0.036	0.041	0.055	0.060
LH	0.008	0.008	0.010	0.016	0.023	0.032	0.056	0.059	0.059
MN	0.018	0.018	0.020	0.026	0.028	0.032	0.040	0.041	0.042
PV	0.014	0.014	0.014	0.014	0.021	0.030	0.037	0.038	0.038
VJ	0.008	0.009	0.010	0.014	0.015	0.019	0.030	0.038	0.040
VR	0.009	0.009	0.015	0.024	0.029	0.036	0.046	0.079	0.092
ZJ	0.009	0.009	0.010	0.014	0.018	0.031	0.039	0.049	0.051
Guadalajara	0.008	0.009	0.010	0.014	0.019	0.027	0.040	0.054	0.056
Leonina	0.008	0.009	0.011	0.021	0.026	0.035	0.056	0.060	0.060
Verghereto	0.009	0.009	0.017	0.024	0.029	0.036	0.044	0.077	0.092

**TABLE 7** Data used as input for calculating the position of the threshold curve: The values of cohesion were used for obtaining a perfect match between the  $k_{1st}$  value and the one calculated with Equation (21). When cohesion was nil (i.e., when the amount of clay was lower than 0.05) then the  $\rho$ -value of the representative grain was used for the fine tuning of the two  $k$ -values. The shape 'rounded' was chosen when the material was eroded mostly as soil aggregates or sand grains (smallest  $D_{50}$  size)

Site code	RFC average (kg/kg)	$D_{50}$ (m)	$\Delta\rho$ (kg/m <sup>3</sup> )	Cohesion (Pa)	$\varphi_{50}$ (deg)	Pervailing grain shape	Average $R_{tot}$ intensity (Pa) <sup>c</sup>
VJ	0.256	0.0005	1300	95.4	61.2	angular	90.3
HE	0.255	0.00014	1300	152	56.9	int/ang	145.0
PV	0.66	0.012	1000 <sup>a</sup>	34	32.5	rounded	113.5
ZJ	0.335	0.00037	1300	87.5	61.2	angular	82.0
VR	0.81	0.005	1210 <sup>b</sup>	0	61.2	angular	104.3
MN	0.9	0.007	1250 <sup>b</sup>	0	61.2	angular	154.5
LH	0	0.00002	50	82	32.5	rounded	129.3
LB	0	0.00002	200	113.5	32.5	rounded	93.7

<sup>a</sup>This was the site showing the most advanced weathering.

<sup>b</sup>The measured saturated bulk density was 2248 kg/m<sup>3</sup>.

<sup>c</sup>In the observed gradient range.

values for the different badland sites are plotted with black triangle in Figure 11 with the solid symbols depicting the dispersive soils at the LH and LB sites. Additionally, in Figure 11, open red circles report the  $FS_{ratio}$  calculated for the non-dispersive badland soils and the red dashed curve show the corresponding best fitting equation and the relative  $R^2$  value. Such relation, which is significant at a 0.01 level, seems to suggest that we can rely on Smedon and Beasley (1961) relation or on its improvements, at least for non-dispersive soils.

### 3.2 | Badland thresholds characterization

In order to investigate the effects of RFC on the resistance to the GH regression ( $k$ -value), the RFC by mass and RFC cover data for the GH sites have been classified into five equally spaced RFC classes and plotted against their corresponding  $k$  values ranges. Leonina data have been omitted in this analysis due to its extremely diversified lithological characteristics, being over consolidated marine dispersive silty-clay to clayey silt sediments without any type of cement, while the others are mostly cemented or partly cemented sediments with distinct layering. Figure 12 shows a slight increase of  $k$  in relation to the increase of RFC. The trend is better shown if the RFC is by mass, where the effect of RFC tends to a horizontal asymptote. When RFC is given by visual estimation then a slight decrease is shown after a peak at about [60, 80].

### 3.3 | Curve Number value selection for badlands

Once the distribution of the  $k$ -values for each study site was established, a possible CN value and the derived  $S_{0.05}$  (i.e., depending on the land use and vegetation) parameter for each site was identified in order to evaluate if the badland GH data do agree with the  $k_{1st}$  model first proposed by Torri and Poesen (2014) and then further developed by Torri, Poesen, et al. (2018). With this aim in mind, the CN values and possibly how these change with vegetation type and cover need to be defined.

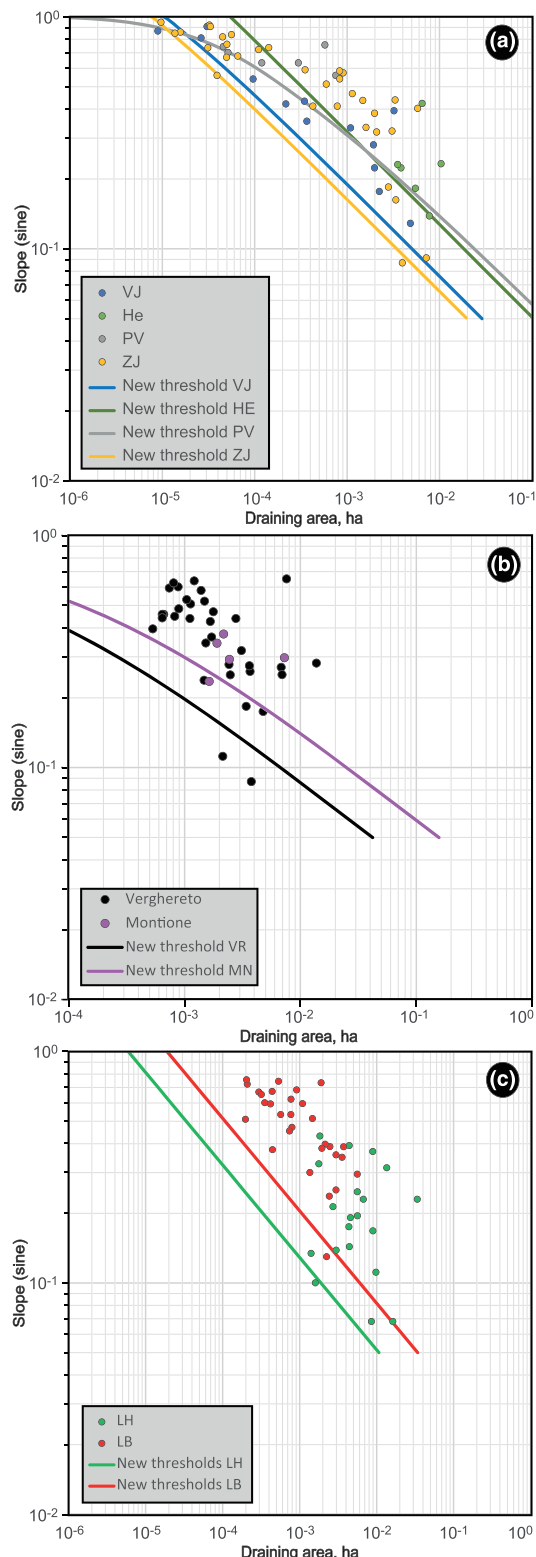
For this purpose, a criterion was used that is explained and motivated in the following lines. A first observation is that all the sites are characterized by soils either very eroded or at the early stages of weathering (i.e., surficial alterite or regolith horizons). Generalizing,

where rills and gullies develop the soil is usually less protected by vegetation and often stressed by grazing animals or by machinery transiting, soil digging or tilling both for agriculture of any type of land-use adjustment. These lead land-use CN values towards high values (locally poor hydrologic condition, see CN-runoff methodology). Regarding the experimental sites presented here, the first 50 cm of the soil profile are usually interrupted by an impervious layer, hence these soils can be classified as hydrologic soil group D. As shown in Table 3 the soil is almost bare: the only value recommended in the standard CN tables is a CN value close to 92–94 (i.e., corresponding to bare fallow), which obviously does not cover all the facets of the land-use types that are found in badlands or more generally, around any highly eroded site. For these reasons, data and relationships derived for rangeland conditions (hence comprehensive of grazing and overgrazing situations) were added. The CN values were derived using relations between CN and vegetation cover ( $V_c$ ) proposed in the literature (see Section 2.5). For all GH sites CN values were first calculated. Then, only those CN values derived for similar climatic and land-use conditions were considered (shaded values in Table 8). The climatic parameters classify the Spanish sites close to the United States situation while the Italian one is somewhat farther because of the larger annual precipitation amount. For these reasons, the relations proposed by Descheemaeker et al. (2008), being derived for monsoon climate, are not applicable. The final CN values in Table 8 were estimated averaging the different CN values calculated with the selected equations.

To compare the  $k_{1st}$  values determined with data observed in the field with  $S_{0.05}$  as proposed by Torri and Poesen (2014) and Torri, Poesen, et al. (2018),  $\psi$  factors also need to be considered because values are different from one for the different test sites.

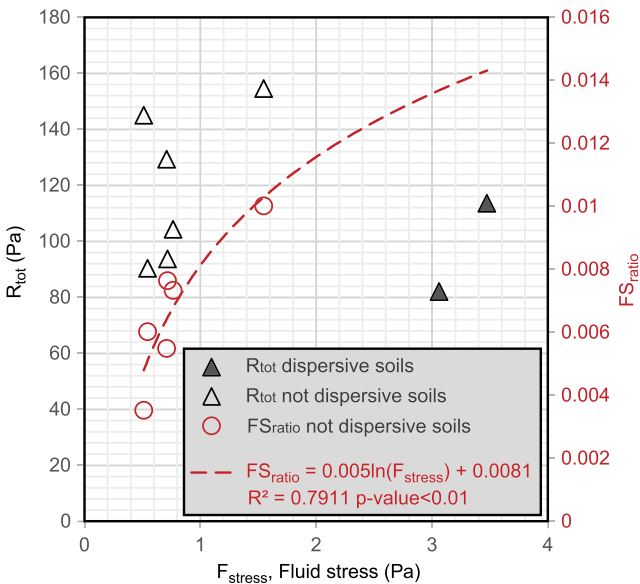
### 3.4 | The $\psi$ factor

Table 8 shows the steps taken to obtain the  $S_{0.05}$  parameter (Equation 17). Table 9 contains the  $S_{0.05}$ , the  $\psi$  factor and the observed  $k_{1st}$  (Equation 17). The  $\psi$  factor has so far not yet been discussed. The  $\psi$  factor accounts for the local effects of processes that may be important in a site but absent in another. For instance, such effects can be related to the presence of joints or faults ( $\psi = 0.76$



**FIGURE 10** Soil surface slopes ( $\sin\theta$ ) at the gully heads and their corresponding catchment areas (a) measured in the different badland study areas (see Table 2). [Color figure can be viewed at [wileyonlinelibrary.com](http://wileyonlinelibrary.com)]

from Torri and Poesen [2014]). In addition, there is another correction factor for the bare slopes of the biancanas in the Leonina site (LB) which was derived by laboratory experiments discussed by Torri et al. (1994). This factor accounts for the over-consolidation of silty clay marine sediment biancana deposits, which are characterized by a very high resistance to erosion when dry but which drops to almost



**FIGURE 11:** The  $\bar{F}_{stress}$  and  $R_{tot}$  values for the studied badland sites (black triangles). Solid triangles are relative to the Leonina site (LH and LB) where the clay soil has a dispersive character. Open red circles report the  $FS_{ratio}$  calculated for the non-dispersive badland soils with the red dashed curve being the corresponding best fitting equation. [Color figure can be viewed at [wileyonlinelibrary.com](http://wileyonlinelibrary.com)]

zero when thoroughly wet. The boundary line between the erodible phase (topsoil) and the still too resistant subsoil layer, moves slowly into this sediment at a very low velocity, which corresponds to the velocity of the water front penetration ( $u_{wfp}$ ). This rate is smaller than the rate at which the erodible layer is potentially eroded, that is its potential denudation rate ( $d_{pr}$ ). When the erosion is driven by raindrop impact and sheet flow dominates,  $d_{pr} < u_{wfp}$ , but whenever concentrate flow erosion occurs, it cannot erode at a rate that is larger than  $u_{wfp}$  and the flow detachment is substantially limited.

A similar situation is observed in the two sites VR and MN, with VR characterized by a deeper surface alterite layer than the MN site due to peculiar geological conditions. These two sites are characterized by similar lithologies, predominantly constituted of regular alternations of sandstone and pelitic marls (i.e., siltstone and mudstone, see Table 3) but with different layer bedding orientations with respect to the slope geometry. Indeed, badlands in the Verghereto area (Figure 13a-d) developed mainly on an anaclinal slope setting (i.e., with bedding dipping into the slope), while those in the Montione site (Figure 13e-h) developed on a cataclinal dip slope setting (i.e., with bedding dip angle [sub]parallel to the local terrain gradient) (Santangelo et al., 2015). In the Verghereto sites, the soil surface is characterized by a thick, highly fragmented layer of small rock fragments (0.5–5 cm) with a variable depth, while in the Montione site a thin layer of fragments (i.e., centimetric) overlaps a more resistant continuous layer parallel to the surface. The thickness and the mechanical characteristics of the surface layers at the two badland sites are different and influence the overall availability of incoherent material, the infiltration, runoff and runon pathways that together control the gully initiation and development. The Verghereto situation favours the formation of a layer of small rock fragments and fine earth materials, over layers which offer routes for water to infiltrate (pore systems along the contact between layers which are directed with an

**FIGURE 12** Variability of  $k$  values (Equation 10) for different rock fragment content (RFC) by mass (a) and RFC cover classes (b) represented by different colours. [Color figure can be viewed at [wileyonlinelibrary.com](http://wileyonlinelibrary.com)]

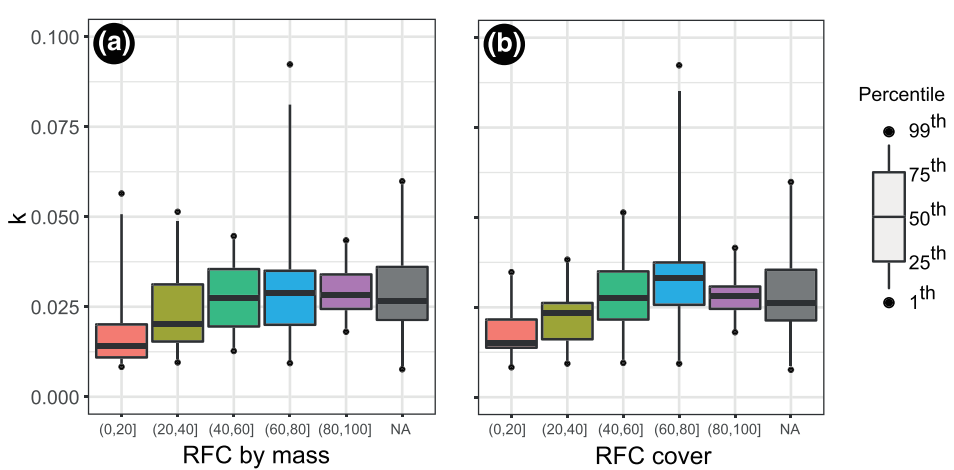


**TABLE 8** Estimates of Curve Number (CN) values for each study sites using relations based on vegetation cover reported in Section 2.5

CN values estimated from CN –  $V_c$  equations (see Section 3.5)

Site code	$V_c$	Equation (fA1a)	Equation (fA1b)	Equation (fA1c)	Equation (fA1d)	Equation (fA1e)	Equation (fA1f)	Equation (fA1g)
PV	0.016	90.7	99	94.8	93.4*	92.9*	90.8	86.7*
HE	0.5	74.3	75.5	89.25	85.8*	90*	84.5	76.5
VJ	0.034	90.3	99	94.6*	93.1*	92.8*	90.6	86.3
ZJ	0.059	89.8	99	94.32*	92.68*	92.65*	90.23	85.76
VR	0.03	90.4	99	94.7	93.1*	92.8	90.6*	86.4*
MN	0.03	90.4	99	94.7*	93.1	92.8	90.6*	86.4*
LH	0.15	87.7	99	93.3*	91.3*	92.1*	89.1*	83.9
LB	0.02	90.6	99	94.8*	93.3*	92.9*	90.7	86.6

Note: The asterisk (\*) highlights CN values derived for similar climatic and land-use conditions.

**TABLE 9** Final values of Curve Number (CN) and  $S_{0.05}$  calculated for the different gully head (GH) sites obtained with row averages of values in shaded columns corresponding to the vegetation characteristics ( $V_c$ ) of the corresponding GH sites (see Table 8). The  $\psi$  factor values account for various factors adding or reducing resistance to GH formation, for example in presence of joints  $\psi = 0.76$  (Equation (17), Torri & Poesen, 2014), and other local characteristics, such as the water penetration front rate as limiting factor for erosion to proceed, that is  $\psi = 3.5$  (Torri et al., 1994, 2018a)

Final averaged parameter values (for Equations (25) and (26)) <sup>b</sup> based on selected values [values with asterisk (*) in Table 8]						
Site code	CN average	Resulting $S_{0.05}$	$\psi$ Factor	$k_{1st}$ Observed	$k_{1st}$ Calculated	$k_{1st}$ Observed/ $k_{1st}$ calculated ( $k_{ratio}$ )
PV	91.9	29.14	1	0.014	0.0108	1.297
HE	88.4	46.4	1	0.02	0.0247	0.809
VJ	93.5	22.3	1	0.009	0.0066	1.359
ZJ	93.2	23.4	1	0.009	0.0073	1.236
VR	92.1	28.4	0.76	0.009	0.0078	1.148
MN	91.2	32.5	0.76 ( $\times 1.31$ ) <sup>a</sup>	0.018	0.0172	1.045
LH	91.4	31.4	0.76	0.008	0.0094	0.848
LB	93.6	21.6	2.66	0.013	0.0167	0.779

<sup>a</sup>MN site should be corrected by two different site specific  $\psi$ -values: the one between brackets, due to geologic layer dip, was not used because unsufficiently studied (see text).

<sup>b</sup>Equations (24) and (26) (see Section 1.1) correspond, respectively, to Equations (17) and (18) where the RFC effect is ignored ( $RFC_{eff} = 1$ ).

important component being normal to the surface slope). Conversely, the Montione situation is dominated by the presence of a layer parallel to the slope surface, hence quite impervious to infiltration. This slows down the velocity at which the layers weather into rock fragments, while the water which infiltrates into the surface rock

fragment layer, cannot infiltrate deeper, quickly resurfaces contributing to surface runoff. As a consequence, the surface rock fragments at the Montione site are removed at a speed which is larger than the speed of new rock fragment formation, while in Verghereto the situation seems to be totally opposite with a surface rock fragment layer

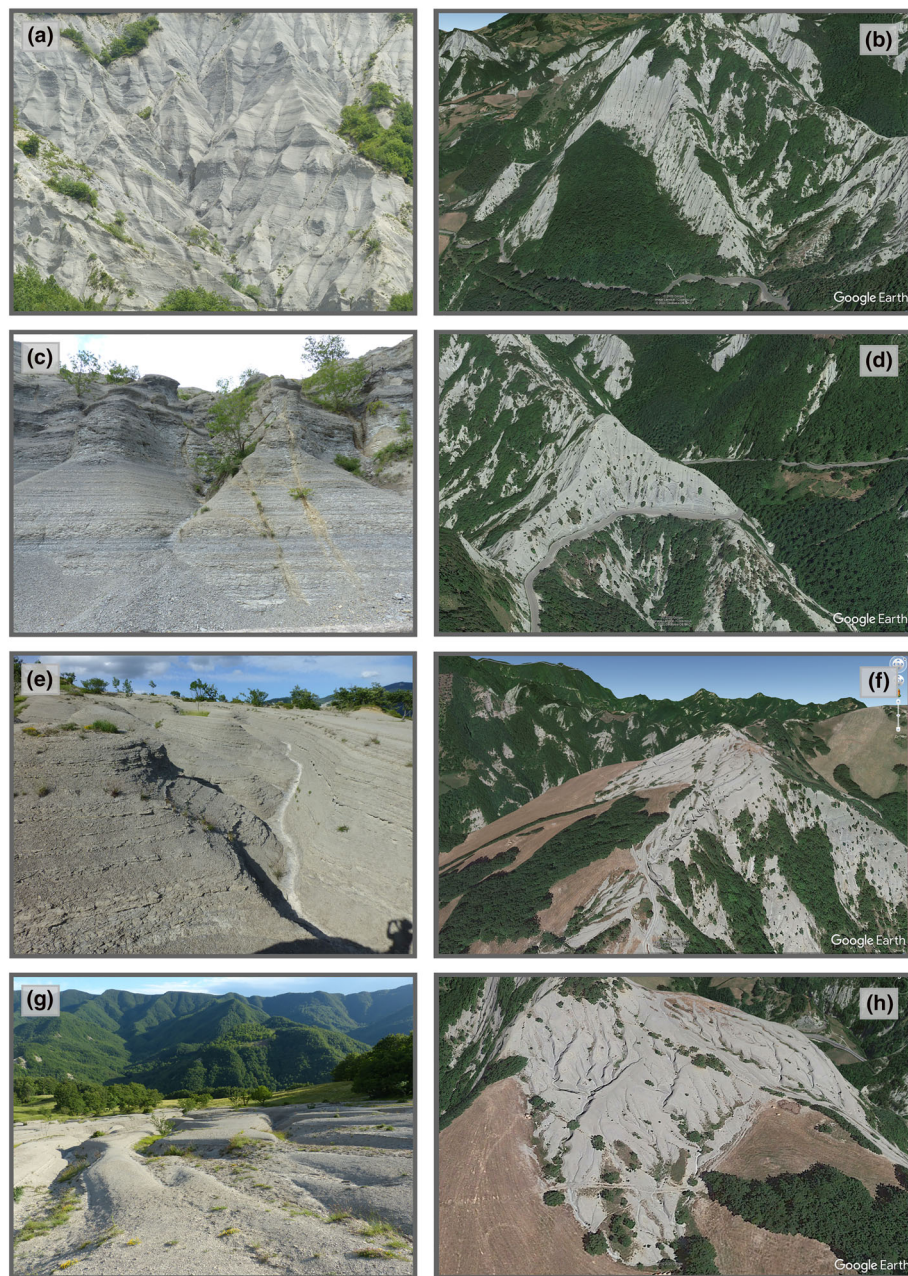


**FIGURE 13** Badland development in relation to layer bedding orientation in the Verghereto (a,b,c,d) and in the Montione (e,f,g,h) study sites. [Color figure can be viewed at [wileyonlinelibrary.com](http://wileyonlinelibrary.com)]

produced more rapidly than can be eroded. Therefore, the gullies at Montione are detachment-limited in contrast to Verghereto where transport-limited conditions prevail. This indicates that the GH predictions at Montione should be corrected by a  $\psi$  factor in between 1.5 and 2. At this moment we do not have independent data to confirm this statement. Consequently, we applied the joint-fault correction factor where joints were observed and the detachment rate correcting factor for the Leonina badlands (LB) because supported by independent laboratory data, leaving the Montione badlands without correction for limited erodibility.

### 3.5 | The land-use interpolating function ( $S_{0.05}$ )

Torri, Poesen, et al. (2018) suggested a slightly different equation than the one suggested previously (Torri & Poesen, 2014) for including the land-use effect using  $S_{0.05}$ . As the badlands  $k_{1st}$  data are among the smallest values recorded, these can be compared and two

interpolating functions identified and evaluated. The two equations, ignoring RFC effects ( $RFC_{eff} = 1$ ), become:

$$k_{1st} = 0.00124\psi(S_{0.05} - 30) \quad (25)$$

and

$$k_{1st} = 0.00113\psi[1 - \exp(-0.0137S_{0.05})]S_{0.05} \quad (26)$$

with  $k_{1st}$  in  $ha^{-0.4}$ ,  $S_{0.05}$  in millimetres and  $\psi$  the corrector factors reported in Table 8.

The  $k_{1st}$  values calculated using Equation (26) are reported in Table 7. Given the importance of the  $\psi$  factor values, the ratio  $\frac{k_{1st}}{\psi}$  is plotted versus  $S_{0.05}$  in Figure 14. Figure 14 shows how the data fit the two curves (Equations 25 and 26). The only datum that clashes with the Torri, Poesen, et al. (2018) curve is the one indicated with a green cross overlapping a small red circle. If we accept this curve then this

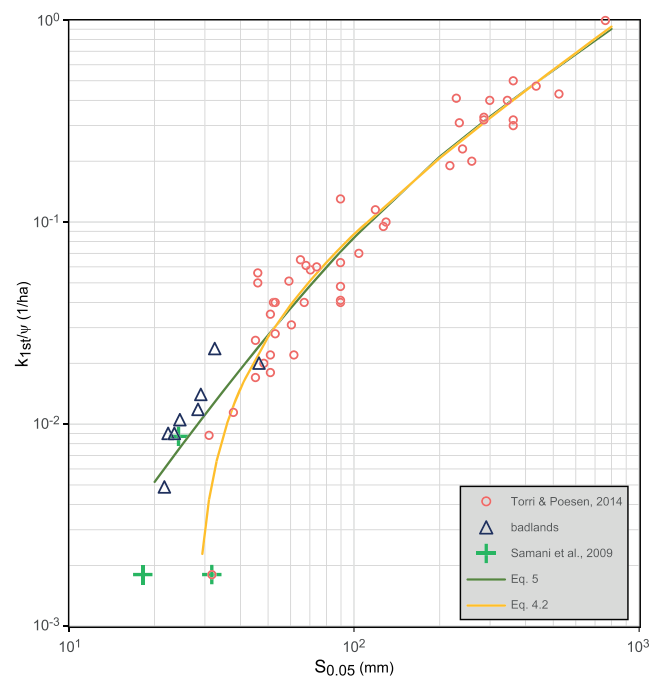


**FIGURE 14** Ratio  $k_{1st}$  versus  $S_{0.05}$  for badlands (triangles). The green crosses depict the same data for cropland (lower value) and rangeland (Nazari Samani et al., 2009), while the red circles are data reported in Torri and Poesen (2014). Solid green line and dashed orange line, show respectively the interpolating fitting Equations (25) and (26). [Color figure can be viewed at [wileyonlinelibrary.com](http://wileyonlinelibrary.com)]

datum should be considered as an outlier, either because there was an error in reporting it or due to some local peculiarities. Hence, the Nazari Samani et al. (2009) data (green crosses in Figure 14) were re-examined. These reported data are for cropland (a very small group) and rangeland. The latter were not used by Torri and Poesen (2014), but they now are included in this analysis. For this purpose, data reported in the original article were digitized and the  $k_{1st}$  values calculated for rangeland and cropland, the latter being in total agreement with Torri and Poesen (2014) data. The values of  $S_{0.05}$  were calculated following the methodology proposed in the material and methods section, obtaining a different value for the  $S_{0.05}$  for cropland. The difference between the two evaluations of the CN and hence  $S_{0.05}$  values for cropland, was not due to the methodology. It is related mainly to another paper by Nazari Samani et al. (2016), where they conducted runoff experiments on plots for cropland, abandoned, and rangeland soils in the same locality. The photographs showed that the cropland soil was bare, crusted and probably also with a biological crust (lichens or cyanobacteria). This pushes the CN values further towards the largest values, and consequently  $S_{0.05}$  towards very low values. The two recalculated data points are shown in Figure 14 with green crosses. Now also the data reported by Nazari Samani et al. (2009) along with the other data plots very close to the Torri, Poesen, et al. (2018) interpolating curve and support the finding that the Torri and Poesen (2014) Equation (25) must be abandoned.

### 3.6 | Insight on rock fragment content effects

The data reported in Table 9 relative to badland sites, allow to calculate the effect of rock fragments on the ratios ( $k_{ratio}$ ) between

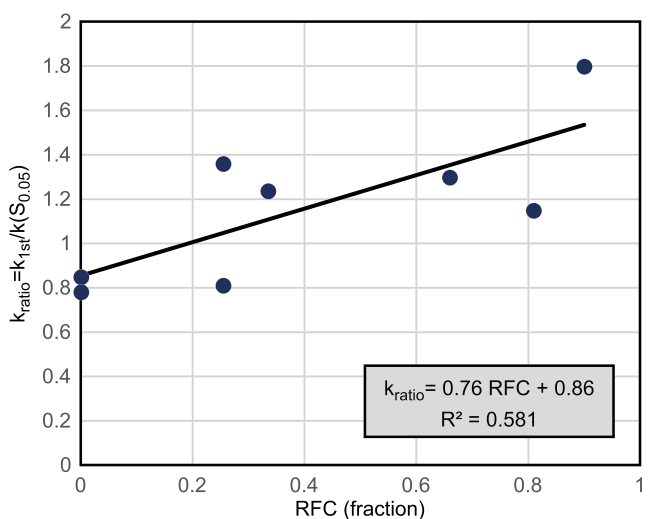


**FIGURE 15** The ratio ( $k_{ratio}$ ) between the  $k_{1st}$  observed and the  $k_{1st}$  calculated as a function of  $S_{0.05}$  alone is plotted versus the rock fragment content (RFC) by mass at the studied badland sites. Calculated  $k_{1st}$  values were obtained using Equation (26). [Color figure can be viewed at [wileyonlinelibrary.com](http://wileyonlinelibrary.com)]

measured and predicted  $k_{1st}$  values. The comparison of the predicted  $k_{1st}$  values without RFC effect with those including a correction for RFC are shown Figure 14. For this comparison, the  $k_{ratio}$  values were obtained considering Equations (26) and (18). If the  $k_{ratio}$  equals 1.0 then there is no RFC effect. If the ratio shows an increasing trend with RFC then there is an RFC effect and the function interpolating the data can be multiplied by the  $k$  calculated with Equation (26) to obtain the best estimate of the measured  $k_{1st}$ .

Note that the ratio is one at an RFC larger than zero because the  $k_{1st}$  reflects the average rock fragment cover over the 55 gully sites used in Figure 14 (average RFC between 0.1 and 0.3).

As shown in Figure 15, with increasing RFC values, predicted  $k_{1st}$  values tend to underestimate the measured  $k_{1st}$  values. Overall, the general behaviour of  $k_{ratio}$  suggests an increase of  $k_{1st}$  with RFC. Anyhow, the number and scatter of data do not allow to calculate a reliable model for accounting the effect of RFC.

Most of the variance regarding the threshold model (Equation 26) is explained by the land use as quantified by the CN- $S_{0.05}$  runoff model hence only a relatively small data scatter still remains to be characterized and explained. It is well known that weather and climate data as well as the RFC have an impact on the threshold conditions. This means that it would be better to examine weather/climate and RFC at the same time in order to extract these factors. To do that a much larger data base than the one relative to badlands is obviously needed.

## 4 | CONCLUSIONS

The data presented and discussed in this article extend the GH topographic and land-use thresholds to Mediterranean badlands, whose data align to those discussed by Torri and Poesen (2014).

A strong accent is here posed on the repeatability and reproducibility (RR) of the parameters needed for calculating the gully threshold curves and for characterizing the GH data bases. To ensure this issue, the procedure to assign a CN value to a given representative

land use was improved. It is obvious that under any possible condition, when runoff concentrates, a rill or gully will be initiated when and where the soil/land-use system is the weakest (e.g., scarce vegetation protection, presence of various disturbances, water concentration paths). Hence a land-use type should also be characterized by its weak spots such as animal paths, machinery trails, bare soil patches and not just through its average situation. This results in a selection of CN values representing the poorest hydraulic conditions. A set of equations, linking vegetation cover to CN was collected from the literature for characterizing the conditions at the boundary between a safe, well protected soil situation and a totally bare soil surface, under different types of vegetation. This CN estimation approach reduces arbitrariness and increase the RR of the evaluation of the land-use effect on GH thresholds.

The study also re-evaluated the effects of rock fragments proposing the use of a by mass rather than a visual estimation of rock fragment cover at the soil surface by sampling the top soil over a depth of 5 to 10 cm (depth depending on the grain size of the surface: if rock fragments are less than 5 cm in size then a soil sample of a few centimetres thick is sufficient; for larger rock fragment sizes a soil sample taken over a larger depth is needed).

The local factors, inherited by the geological and the orogenetic history (here mainly joints and local structural attributes) have been shown to affects the threshold curve. These effects still need further studies and confirmation to be safely used in the threshold prediction.

Another aspect that has been addressed is the importance of the history of the area under study: what one observes today is a landscape that was formed under the current conditions, or it may be a legacy of the past centuries or even millennia. The analysis of historical documents provides a better view of the situation under which the gullies at the study sites formed. The analysis of past geoenvironmental records (e.g., paleopalynological data, dendrochronological series, radionuclide data, etc.) may complement such investigations. The conditions for the formation of the currently dormant GHs at the LH study area is the result of past local conditions similar to the ones that the LB study area was experiencing until 40–50 years ago. Similar considerations can be made for Verghereto/Montione and for the Guadalajara sites. In many of these study sites one cannot use the present-day conditions and obtain theoretical  $k$ -values in agreement with the measured  $k$ . History also shows that the cause for these badland sites to develop had mainly anthropogenic drivers while present conditions testify a today abandonment (which is not necessarily the cause of GH formation).

The effect of the rock fragments component on the GH threshold model was confirmed: that is with increasing rock fragment content by mass, the resistance to gully formation increases. Similar confirmations were proposed for the presence of joint networks. Another probable cause of differentiation in threshold values was found due to the layer bedding orientation: while Verghereto badland gullies are almost all formed into a given bedding orientation, the Montione site is characterized by gullies that developed on the opposite bedding.

The GH topographical threshold model gains its present form following studies by Patton and Schumm (1975) and the generalization proposed by Montgomery and Dietrich (1994). The Torri and Poesen (2014) literature review on the Hortonian runoff generated gullies brought the model to a better clarification and included the effects of land use to expand the model from a topography-based to a topography and land-use based one. The often ignored Rossi et al. (2015) paper warns about the bias of the classical approach to calculating

threshold lines. The data collected in this study required an improvement of the model. It was necessary to express the critical flow shear stress explicitly. This was done using a classical soil strength concept with a component depending on a friction term and another on a cohesive term. When cohesion is dominant the topographic threshold line is straight in a  $(A, \sin \gamma)$  bilog representation of the GH conditions. When friction is dominant the threshold line bends at slope gradients above  $60^\circ$ . Hence, the condition for GH initiation and retreat is the result of the tradeoff between the frictional and cohesive components of the resistance forces. Additional studies are needed to completely exploit this new modelling perspective.

## ACKNOWLEDGEMENTS

The authors acknowledge the E-OBS dataset from the EU-FP6 project UERRA (<http://www.uerra.eu>) and the Copernicus Climate Change Service, and the data providers in the ECA&D project (<https://www.ecad.eu>). Additional details can be found in Cornes et al. (2018). The authors thank CNR\_IRPI and KU Leuven for supporting this study. Open Access Funding provided by Consiglio Nazionale delle Ricerche within the CRUI-CARE Agreement.

## AUTHOR CONTRIBUTIONS

Mauro Rossi, Dino Torri and Jean Poesen have made substantial contributions to conception and design of the study. All the authors have made substantial contributions to the data acquisition. Mauro Rossi, Dino Torri, Jean Poesen and Sofie De Geeter have made substantial contributions to data analysis and interpretation and have been involved in drafting the manuscript and revising it critically for important intellectual content. All the authors have given final approval of the version to be published.

## DATA AVAILABILITY STATEMENT

The data that support the findings of this study are available from the corresponding author upon reasonable request.

## ORCID

Mauro Rossi  <https://orcid.org/0000-0002-0252-4321>

## REFERENCES

- Abdel-Rahman, N.M. (1963) The effect of flowing water on cohesive beds (Doctoral dissertation, ETH Zurich).
- Amati, A. (1868) Dizionario corografico dell'Italia.
- Amici, V., Maccherini, S., Santi, E., Torri, D., Vergari, F. & Del Monte, M. (2017) Long-term patterns of change in a vanishing cultural landscape: A GIS-based assessment. *Ecological Informatics*, 37, 38–51. Available from: <https://doi.org/10.1016/j.ecoinf.2016.11.008>.
- Atienza, M.A.P. & Pascua, M.A.R. (2005) *La alfarería de zarzuela de Jadraque: Una guía Para conocerla y apreciarla*. Guadalajara: AACHE Ediciones de Guadalajara.
- Ballesteros Cánovas, J.A., Stoffel, M., Martín-Duque, J.F., Corona, C., Lucía, A., Bodoque, J.M. et al. (2017) Gully evolution and geomorphic adjustments of badlands to reforestation. *Scientific Reports*, 7(1), 45027. Available from: <https://doi.org/10.1038/srep45027>.
- Baltas, E. (2007) Spatial distribution of climatic indices in northern Greece. *Meteorological Applications*, 14(1), 69–78. Available from: <https://doi.org/10.1002/met.7>.
- Beavis, S.G. (2000) Structural controls on the orientation of erosion gullies in mid-western New South Wales, Australia. *Geomorphology*, 33(1–2), 59–72. Available from: [https://doi.org/10.1016/S0169-555X\(99\)00110-5](https://doi.org/10.1016/S0169-555X(99)00110-5).

- Beer, C.E. & Johnson, H.P. (1965) Factors related to gully growth in the deep loess area of Western Iowa. In: Proc. Federal Inter-Agency Sedimentation Conf. US. Dep. of Agric. Misc. Publ. pp. 37–43.
- Biancalani, R. (1988) Stima dei picchi di deflusso idrico su un versante: Messa a punto di un metodo. Università di Firenze.
- Biancalani, R. (1989) Probabilistic nature of entrainment of gravels in concentrated overland flow. *Quaderni di Scienza del Suolo*, II, 131–144.
- Bocco, G. & Valenzuela, C.R. (1993) Integrating satellite-remote sensing and geographic information systems technologies in gully erosion research. *Remote Sensing Reviews*, 7(3–4), 233–240. Available from: <https://doi.org/10.1080/02757259309532179>.
- Branson, F., Gifford, G., Renard, K. & Hadley, R. (1981) *Rangeland hydrology*. Society of Range Management, Range Science Series No. 1. Dubuque, Iowa: Kendall/Hunt Publ. Co..
- Brunori, F., Penzo, M.C. & Torri, D. (1989) Soil shear strength: Its measurement and soil detachability. *Catena*, 16(1), 59–71. Available from: [https://doi.org/10.1016/0341-8162\(89\)90004-0](https://doi.org/10.1016/0341-8162(89)90004-0).
- Calzolari, C., Ristori, J., Busoni, E. & Chiarucci, A. (1993) Morphology development in a'biancana'badland area and relationships with soils and vegetation. Proc. Int. Work. Soil Erosion in Semiarid Mediterranean Areas. Roma 205–216.
- Calzolari, C., Ristori, J., Sparvoli, E., Chiarucci, A. & Soriano, M. (1993) Soils of biancana badlands: Distribution, characteristics and genesis in Beccanello farm (Tuscany, Italy). *Quaderni di Scienza del Suolo*, 5, 9–142.
- Campo-Bescós, M.A., Flores-Cervantes, J.H., Bras, R.L., Casalí, J. & Giráldez, J.V. (2013) Evaluation of a gully headcut retreat model using multitemporal aerial photographs and digital elevation models. *Journal of Geophysical Research - Earth Surface*, 118(4), 2159–2173. Portico. Available from: <https://doi.org/10.1002/jgrf.20147>.
- CCI/CLIVAR/JCOMM Expert Team on Climate Change Detection and Indices (ETCCDI). (2020) Indices dictionary [WWW Document]. <https://www.ecad.eu/>. URL <https://www.ecad.eu/indicesextremes/indicesdictionary.php> [Accessed 2th April 2020].
- Chiarucci, A., De Dominicis, V., Ristori, J. & Calzolari, C. (1995) Biancana badland vegetation in relation to morphology and soil in Orcia valley, Central Italy. *Phytocoenologia*, 25(1), 69–87. Available from: <https://doi.org/10.1127/phyto/25/1995/69>.
- Chiaverini, I., Colica, A., Del Sette, M. & Ostuni, D. (1999) Misura dell'erosione: Metodi fotogrammetrici applicati in alcune aree argillose dell'Alta Val d'Orcia. *Geologia Tecnica e Ambientale*, 74, 295–303.
- Colica, A. & Guasparri, G. (1990) Sistemi di fratturazione nelle argille plioceniche del territorio senese. *Implicazioni Geomorfologiche*, 15, 29–36.
- Conoscenti, C., Agnesi, V., Angileri, S., Cappadonia, C., Rotigliano, E. & Märker, M. (2013) A GIS-based approach for gully erosion susceptibility modelling: a test in Sicily, Italy. *Environmental Earth Sciences*, 70(3), 1179–1195. Available from: <https://doi.org/10.1007/s12665-012-2205-y>.
- Cornes, R.C., van der Schrier, G., van den Besselaar, E.J.M. & Jones, P.D. (2018) An ensemble version of the E-OBS temperature and precipitation data sets. *Journal of Geophysical Research - Atmospheres*, 123(17), 9391–9409. Available from: <https://doi.org/10.1029/2017JD028200>.
- De Baets, S., Poesen, J., Knapen, A., Barberá, G.G. & Navarro, J.A. (2007) Root characteristics of representative Mediterranean plant species and their erosion-reducing potential during concentrated runoff. *Plant and Soil*, 294(1–2), 169–183. Available from: <https://doi.org/10.1007/s11104-007-9244-2>.
- De Baets, S., Torri, D., Poesen, J., Salvador, M.P. & Meersmans, J. (2008) Modelling increased soil cohesion due to roots with EUROSEM. *Earth Surface Processes and Landforms*, 33(13), 1948–1963. Available from: <https://doi.org/10.1002/esp.1647>.
- De Geeter, S. (2018) Topographic thresholds for gully channel heads in Mediterranean badlands and sunken lanes in loess areas (Master Thesis). Katholieke Universiteit Leuven, Leuven.
- De Martonne, E. (1942) NOUVELLE CARTE MONDIALE DE L'INDICE D'ARIDITÉ (CARTE hors texte). *Annales de Géographie*. JSTOR, 51(288), 241–250. Available from: <https://doi.org/10.3406/geo.1942.12050>.
- De Ploey, J. (1992) Gullyling and the age of badlands: An application of the erosional susceptibility model Es. *Catena. Supplement (Giessen)*, 23(1–4), 31–45.
- Descheemaeker, K., Poesen, J., Borselli, L., Nyssen, J., Raes, D., Haile, M. et al. (2008) Runoff curve numbers for steep hillslopes with natural vegetation in semi-arid tropical highlands, northern Ethiopia. *Hydrological Processes*, 22(20), 4097–4105. Available from: <https://doi.org/10.1002/hyp.7011>.
- Dewilde, L. (1986) Studie can de competentie van stroming in geulen in functie van hellings, debiet en beddingsruwheid. Unpubl. M. Sc. thesis, KU Leuven.
- Doumit, J.A. & Awad, S.F. (2019) Drone-based DSM for multiscale geometrical characteristics of ephemeral gullies. *International Journal of Advanced Research and Publications*, 3, 83–88.
- Espejo Serrano, R. (1985) The ages and soils of two levels of "raña" surfaces in Central Spain. *Geoderma*, 35(3), 223–239. Available from: [https://doi.org/10.1016/0016-7061\(85\)90039-4](https://doi.org/10.1016/0016-7061(85)90039-4).
- Fiorucci, F., Ardizzone, F., Rossi, M. & Torri, D. (2015) The use of stereoscopic satellite images to map rills and ephemeral gullies. *Remote Sensing*, 7(10), 14151–14178. Available from: <https://doi.org/10.3390/rs71014151>.
- Fitzjohn, C., Ternan, J.L. & Williams, A.G. (1998) Soil moisture variability in a semi-arid gully catchment: Implications for runoff and erosion control. *Catena*, 32(1), 55–70. Available from: [https://doi.org/10.1016/S0341-8162\(97\)00045-3](https://doi.org/10.1016/S0341-8162(97)00045-3).
- Frankl, A., Stal, C., Abraha, A., Nyssen, J., Rieke-Zapp, D., De Wulf, A. et al. (2015) Detailed recording of gully morphology in 3D through image-based modelling. *Catena*, 127, 92–101. Available from: <https://doi.org/10.1016/j.catena.2014.12.016>.
- Frich, P., Alexander, L., Della-Marta, P., Gleason, B., Haylock, M., Klein Tank, A. et al. (2002) Observed coherent changes in climatic extremes during the second half of the twentieth century. *Climate Research*, 19, 193–212. Available from: <https://doi.org/10.3354/cr019193>.
- Govers, G., Takken, I. & Helming, K. (2000) Soil roughness and overland flow. *Agronomie*, 20(2), 131–146. Available from: <https://doi.org/10.1051/agro:2000114>.
- Grieser, J. (2006) *New LocClim 1.10—Local climate estimator*. Rome: FAO.
- Gutierrez-Elorza, M., Garcia-Ruiz, J.M., Garcia, J.L.G., Gutierrez-Santolalla, F., Marti, C., Martin-Errano, A., et al. (2002) In: Gibbons, W. & Moreno, T. (Eds.) *Quaternary, the geology of Spain*. London: Geological Society of London.
- Gyssels, G., Poesen, J., Bochet, E. & Li, Y. (2005) Impact of plant roots on the resistance of soils to erosion by water: a review. *Progress in Physical Geography: Earth and Environment*, 29(2), 189–217. Available from: <https://doi.org/10.1191/0309133305pp443ra>.
- Hauge, C. (1977) *Soil erosion definitions*. California Department of Forestry.
- Hawkins, R., Ward, T., Woodward, D. & Van Mullem, J. (2009) *Curve number hydrology: State of practice*, 106. Reston, VA: ASCE.
- James, L.A., Watson, D.G. & Hansen, W.F. (2007) Using LiDAR data to map gullies and headwater streams under forest canopy: South Carolina, USA. *Catena*, 71(1), 132–144. Available from: <https://doi.org/10.1016/j.catena.2006.10.010>.
- Joshi, V.U. (2014) The Chambal Badlands. In: Kale, V.S. (Ed.) *Landscapes and landforms of India, world geomorphological landscapes*. Dordrecht: Springer Netherlands, pp. 143–149.
- Joshi, V.U. & Nagare, V.B. (2013) Badland formation along the Pravara River, Western Deccan, India. Can neotectonics be the cause? *Zeitschrift für Geomorphologie*, 57(3), 349–370. Available from: <https://doi.org/10.1127/0372-8854/2013/0109>.
- Kottek, M., Grieser, J., Beck, C., Rudolf, B. & Rubel, F. (2006) World map of the Köppen-Geiger climate classification updated. *Meteorologische Zeitschrift*, 15(3), 259–263. Available from: <https://doi.org/10.1127/0941-2948/2006/0130>.
- Langbein, W.B. & Schumm, S.A. (1958) Yield of sediment in relation to mean annual precipitation. *Eos, Transactions American Geophysical Union*, 39(6), 1076–1084. Available from: <https://doi.org/10.1029/TR039i006p01076>.
- Maccherini, S., Chiarucci, A. & De Dominicis, V. (2000) Structure and species diversity of *Bromus erectus* grasslands of biancana badlands. *Belgian Journal of Botany*, 133, 3–14.

- Mararakanye, N. & Nethengwe, N.S. (2012) Gully features extraction using remote sensing techniques. *South African Journal of Geomatics*, 1, 109–118.
- Martín-Moreno, C., Fidalgo Hijano, C., Martín Duque, J.F., González Martín, J.A., Zapico Alonso, I. et al. (2014) The Ribagorda sand gully (east-Central Spain): Sediment yield and human-induced origin. *Geomorphology*, 224, 122–138. Available from: <https://doi.org/10.1016/j.geomorph.2014.07.013>.
- Meerkerk, A., van Wesemael, B. & Cammeraat, E. (2008) Water availability in almond orchards on marl soils in southeast Spain: The role of evaporation and runoff. *Journal of Arid Environments*, 72(12), 2168–2178. Available from: <https://doi.org/10.1016/j.jaridenv.2008.06.017>.
- Milighetti, M., Monaco, P. & Checconi, A. (2009) Caratteristiche sedimentologico-ichnologiche delle unità silicoclastiche oligo-mioceniche nel transetto Pratomagno–Verghereto, Appennino Settentrionale. *Annali dell'Università Degli Studi di Ferrara, Museologia Scientifica e Naturalistica*, 5, 23–129.
- Molina Ballesteros, E. & Cantano Martín, M. (2002) Study of weathering processes developed on old piedmont surfaces in Western Spain: New contributions to the interpretation of the “Raña” profiles. *Geomorphology*, 42(3–4), 279–292. Available from: [https://doi.org/10.1016/S0169-555X\(01\)00091-5](https://doi.org/10.1016/S0169-555X(01)00091-5).
- Montgomery, D.R. & Dietrich, W.E. (1994) Landscape dissection and drainage area-slope thresholds.
- Nachtergaele, J., Poesen, J., Sidorchuk, A. & Torri, D. (2002) Prediction of concentrated flow width in ephemeral gully channels. *Hydrological Processes*, 16(10), 1935–1953. Available from: <https://doi.org/10.1002/hyp.392>.
- Nazari Samani, A., Ahmadi, H., Jafari, M., Boggs, G., Ghoddousi, J. & Malekian, A. (2009) Geomorphic threshold conditions for gully erosion in southwestern Iran (Boushehr-Samal watershed). *Journal of Asian Earth Sciences*, 35(2), 180–189. Available from: <https://doi.org/10.1016/j.jseas.2009.02.004>.
- Nazari Samani, A., James Wasson, R., Rahdari, M.R. & Moeini, A. (2016) Quantifying eroding head cut detachment through flume experiments and hydraulic thresholds analysis. *Environment and Earth Science*, 75(21), 1424. Available from: <https://doi.org/10.1007/s12665-016-6183-3>.
- Nearing, M. (1991) A probabilistic model of soil detachment by shallow turbulent flow. *Transactions of ASAE*, 34(1), 0081–0085. Available from: <https://doi.org/10.13031/2013.31627>.
- Nearing, M., Simanton, J., Norton, L., Bulygin, S. & Stone, J. (1999) Soil erosion by surface water flow on a stony, semiarid hillslope. *Earth Surface Processes and Landforms: The Journal of the British Geomorphological Research Group*, 24(8), 677–686. Available from: [https://doi.org/10.1002/\(SICI\)1096-9837\(199908\)24:8<677::AID-ESP981>3.0.CO;2-1](https://doi.org/10.1002/(SICI)1096-9837(199908)24:8<677::AID-ESP981>3.0.CO;2-1).
- Parkner, T., Page, M., Marden, M. & Marutani, T. (2007) Gully systems under undisturbed indigenous forest, East Coast region, New Zealand. *Geomorphology*, 84(3–4), 241–253. Available from: <https://doi.org/10.1016/j.geomorph.2006.01.042>.
- Patton, P.C. & Schumm, S.A. (1975) Gully erosion, northwestern Colorado: A threshold phenomenon. *Geology*, 3(2), 88–90. Available from: [https://doi.org/10.1130/0091-7613\(1975\)3<88:GENCAT>2.0.CO;2](https://doi.org/10.1130/0091-7613(1975)3<88:GENCAT>2.0.CO;2).
- Pérez, E. & García, P. (2017) Monitoring soil erosion by raster images: From aerial photographs to drone taken pictures. *European Journal of Geography*, 8, 116–128.
- Pilar Salvador Sanchis, M., Torri, D., Borselli, L., Bryan, R., Poesen, J., Yañez, M.S. & Cremer, C. (2009) Estimating parameters of the channel width-flow discharge relation using rill and gully channel junction data. *Earth Surface Processes and Landforms*, 34(15), 2023–2030. Available from: <https://doi.org/10.1002/esp.1887>.
- Poesen, J.W.A., Torri, D.B. & Vanwalleghem, T. (2011) Gully Erosion: Procedures to Adopt When Modelling Soil Erosion in Landscapes Affected by Gullyling. In: Morgan, R.P.C. & Nearing, M.A. (Eds.) *Handbook of erosion modelling*. Chichester, UK: John Wiley & Sons, Ltd, pp. 360–386.
- Poesen, J. (2017) Soil erosion in the Anthropocene: Research needs. *Earth Surface Processes and Landforms*, 43(1), 64–84. Portico. Available from: <https://doi.org/10.1002/esp.4250>.
- Poesen, J. & Lavee, H. (1994) Rock fragments in top soils: significance and processes. *Catena*, 23(1–2), 1–28. Available from: [https://doi.org/10.1016/0341-8162\(94\)90050-7](https://doi.org/10.1016/0341-8162(94)90050-7).
- Poesen, J., Nachtergaele, J., Verstraeten, G. & Valentim, C. (2003) Gully erosion and environmental change: importance and research needs. *Catena*, 50(2–4), 91–133. Available from: [https://doi.org/10.1016/s0341-8162\(02\)00143-1](https://doi.org/10.1016/s0341-8162(02)00143-1).
- Poesen, J.W.A. & Torri, D. (1989) Mechanisms governing incipient motion of ellipsoidal rock fragments in concentrated overland flow. *Earth Surface Processes and Landforms*, 14(6), 469–480. Available from: <https://doi.org/10.1002/esp.3290140604>.
- Radoane, M., Ichim, I. & Radoane, N. (1995) Gully distribution and development in Moldavia, Romania. *Catena*, 24(2), 127–146. Available from: [https://doi.org/10.1016/0341-8162\(95\)00023-l](https://doi.org/10.1016/0341-8162(95)00023-l).
- Rampoldi, G.B. (1832) *Corografia dell'Italia*: 1. Milano: Fontana.
- Regione Emilia Romagna. (2021) Soil maps and derived thematic maps [WWW Document]. Geological, seismic and soil survey of Emilia Romagna - Soil maps and derived thematic maps. <https://ambiente.regione.emilia-romagna.it/en/geologia/soil/cartography> [Accessed 14th June 2021].
- Repetti, E. (1841) *Dizionario geografico fisico storico della Toscana*.
- Rillig, M.C. & Mumey, D.L. (2006) Mycorrhizas and soil structure. *The New Phytologist*, 171(1), 41–53. Available from: <https://doi.org/10.1111/j.1469-8137.2006.01750.x>.
- Romero, P., Castro, G., Gómez, J.A. & Fereres, E. (2007) Curve Number Values for Olive Orchards under Different Soil Management. *Soil Science Society of America Journal*, 71(6), 1758–1769. Available from: <https://doi.org/10.2136/sssaj2007.0034>.
- Rossi, M., Torri, D. & Santi, E. (2015) Bias in topographic thresholds for gully heads. *Natural Hazards*, 79(S1), 51–69. Available from: <https://doi.org/10.1007/s11069-015-1701-2>.
- Saldaña, A., Ibáñez, J.J. & Zinck, J.A. (2011) Soilscape analysis at different scales using pattern indices in the Jarama–Henares interfluvium and Henares River valley, Central Spain. *Geomorphology*, 135, 284–294. Available from: <https://doi.org/10.1016/j.geomorph.2011.02.016>.
- Santangelo, M., Marchesini, I., Cardinali, M., Fiorucci, F., Rossi, M., Bucci, F. et al. (2015) A method for the assessment of the influence of bedding on landslide abundance and types. *Landslides*, 12(2), 295–309. Available from: <https://doi.org/10.1007/s10346-014-0485-x>.
- Saxton, K.E., Rawls, W.J., Romberger, J.S. & Papendick, R.I. (1986) Estimating generalized soil-water characteristics from texture. *Soil Science Society of America Journal*, 50(4), 1031–1036. Available from: <https://doi.org/10.2136/sssaj1986.0361599500500040039x>.
- Seginer, I. (1966) Gully development and sediment yield. *Journal of Hydrology*, 4, 236–253. Available from: [https://doi.org/10.1016/0022-1694\(66\)90082-5](https://doi.org/10.1016/0022-1694(66)90082-5).
- Shahrivar, A. & Christopher, T. (2012) The effects of soil physical characteristics on gully erosion development in Kohgiloyeh & Boyer Ahmad province, Iran. *Advances in Environmental Biology*, 6(1), 397–406.
- Shruthi, R.B.V., Kerle, N. & Jetten, V. (2011) Object-based gully feature extraction using high spatial resolution imagery. *Geomorphology*, 134(3–4), 260–268. Available from: <https://doi.org/10.1016/j.geomorph.2011.07.003>.
- Sidorchuk, A. (1998) A dynamic model of gully erosion. In: *Modelling soil erosion by water*. Berlin Heidelberg: Springer, pp. 451–460.
- Sidorchuk, A. (1999) Dynamic and static models of gully erosion. *Catena*, 37(3–4), 401–414. Available from: [https://doi.org/10.1016/S0341-8162\(99\)00029-6](https://doi.org/10.1016/S0341-8162(99)00029-6).
- Sidorchuk, A. (2005) Stochastic components in the gully erosion modelling. *Catena*, 63(2–3), 299–317. Available from: <https://doi.org/10.1016/j.catena.2005.06.007>.
- Sidorchuk, A. (2006) Stages in gully evolution and self-organized criticality. *Earth Surface Processes and Landforms*, 31(11), 1329–1344. Available from: <https://doi.org/10.1002/esp.1334>.
- Smerdon, E.T. & Beasley, R.P. (1959) The tractive force theory applied to stability of open channels in cohesive soils. University of Missouri, College of Agriculture, Agricultural Experiment Station, 1959.
- Smerdon, E.T. & Beasley, R.T. (1961) Critical tractive forces in cohesive soils. *Agricultural Engineering*, 42(1), 26–29.
- Suárez, M.C.G. (2008) Metodología de cálculo del factor topográfico, LS, integrado en los modelos Rusle y USped. Aplicación al arroyo del

- lugar, Guadalajara (España). (<http://purl.org/dc/dcmitype/Text>). Universidad Politécnica de Madrid.
- Tabari, H., Hosseinzadeh Talaei, P., Mousavi Nadoushani, S.S., Willems, P. & Marchetto, A. (2014) A survey of temperature and precipitation based aridity indices in Iran. *Quaternary International*, 345, 158–166. Available from: <https://doi.org/10.1016/j.quaint.2014.03.061>.
- Taguas, E.V., Yuan, Y., Licciardello, F. & Gómez, J.A. (2015) Curve Numbers for Olive Orchard Catchments: Case Study in Southern Spain. *Journal of Irrigation and Drainage Engineering*, 141(11), 05015003. Available from: [https://doi.org/10.1061/\(ASCE\)IR.1943-4774.0000892](https://doi.org/10.1061/(ASCE)IR.1943-4774.0000892).
- Ternan, J.L., Williams, A.G., Elmes, A. & Fitzjohn, C. (1996) The effectiveness of bench-terracing and afforestation for erosion control on Raña sediments in Central Spain. *Land Degradation & Development*, 7(4), 337–351. Available from: [https://doi.org/10.1002/\(SICI\)1099-145X\(199612\)7:4<337::AID-LDR238>3.0.CO;2-G](https://doi.org/10.1002/(SICI)1099-145X(199612)7:4<337::AID-LDR238>3.0.CO;2-G).
- Thornes, J.B. (1985) The ecology of erosion. *Geography*, 222–235.
- Torri, D., Biancalani, R. & Poesen, J. (1990) Initiation of motion of gravels in concentrated overland flow: cohesive forces and probability of entrainment. *Catena Supplement*, 17, 79–90.
- Torri, D. & Poesen, J. (1988) Incipient motion conditions for single rock fragments in simulated rill flow. *Earth Surface Processes and Landforms*, 13(3), 225–237. Available from: <https://doi.org/10.1002/esp.3290130304>.
- Torri, D., Colica, A. & Rockwell, D. (1994) Preliminary study of the erosion mechanisms in a biancana badland (Tuscany, Italy). *Catena*, 23(3–4), 281–294. Available from: [https://doi.org/10.1016/0341-8162\(94\)90073-6](https://doi.org/10.1016/0341-8162(94)90073-6).
- Torri, D. & Poesen, J. (2014) A review of topographic threshold conditions for gully head development in different environments. *Earth-Science Reviews*, 130, 73–85. Available from: <https://doi.org/10.1016/j.earscirev.2013.12.006>.
- Torri, D., Poesen, J., Borselli, L., Bryan, R. & Rossi, M. (2012) Spatial variation of bed roughness in eroding rills and gullies. *Catena*, 90, 76–86. Available from: <https://doi.org/10.1016/j.catena.2011.10.004>.
- Torri, D., Poesen, J., Borselli, L. & Knapen, A. (2006) Channel width–flow discharge relationships for rills and gullies. *Geomorphology*, 76(3–4), 273–279. Available from: <https://doi.org/10.1016/j.geomorph.2005.11.010>.
- Torri, D., Poesen, J., Rossi, M., Amici, V., Spennacchi, D. & Cremer, C. (2018) Gully head modelling: A Mediterranean badland case study: Gully head topographic threshold for badlands. *Earth Surface Processes and Landforms*, 43(12), 2547–2561. Available from: <https://doi.org/10.1002/esp.4414>.
- Torri, D., Rossi, M., Brogi, F., Marignani, M., Bacaro, G., Santi, E. et al. (2018) Chapter 4 - Badlands and the Dynamics of Human History, Land Use, and Vegetation Through Centuries. In: Nadal-Romero, E., Martínez-Murillo, J.F. & Kuhn, N.J. (Eds.) *Badlands dynamics in a context of global change*. Amsterdam, Netherlands: Elsevier, pp. 111–153.
- Torri, D., Santi, E., Marignani, M., Rossi, M., Borselli, L. & Maccherini, S. (2013) The recurring cycles of biancana badlands: Erosion, vegetation and human impact. *Catena*, 106, 22–30. Available from: <https://doi.org/10.1016/j.catena.2012.07.001>.
- Torri, D., Sfalanga, M. & Chisci, G. (1987) Threshold conditions for incipient rilling. *Catena Supplement*, 8, 97–105.
- Tucker, G., Lancaster, S., Gasparini, N. & Bras, R. (2001) The channel-hillslope integrated landscape development model (CHILD). In: *Landscape erosion and evolution modeling*. New York: Springer, pp. 349–388.
- USDA & NRCS. (2019) National Engineering Handbook. United States Department of Agriculture (USDA) Natural Resources Conservation Service (NRCS). Part 630 - Hydrology. [WWW Document]. <https://www.nrcs.usda.gov/wps/portal/nrcs/detailfull/national/wntsc/?cid=stelprdb1043063>
- Valentin, C., Poesen, J. & Li, Y. (2005) Gully erosion: Impacts, factors and control. *Catena*, 63(2–3), 132–153. Available from: <https://doi.org/10.1016/j.catena.2005.06.001>.
- Vanmaercke, M., Poesen, J., Van Mele, B., Demuzere, M., Bruynseels, A., Golosov, V. et al. (2016) How fast do gully headcuts retreat? *Earth-Science Reviews*, 154, 336–355. Available from: <https://doi.org/10.1016/j.earscirev.2016.01.009>.
- Vanmaercke, M., Panagos, P., Vanwalleghem, T., Hayas, A., Foerster, S., Borrelli, P. et al. (2021) Measuring, modelling and managing gully erosion at large scales: A state of the art. *Earth-Science Reviews*, 218, 103637. Available from: <https://doi.org/10.1016/j.earscirev.2021.103637>.
- Vrieling, A., Rodrigues, S.C., Bartholomeus, H. & Sterk, G. (2007) Automatic identification of erosion gullies with ASTER imagery in the Brazilian Cerrados. *International Journal of Remote Sensing*, 28(12), 2723–2738. Available from: <https://doi.org/10.1080/01431160600857469>.
- Willgoose, G. (2005) Mathematical modeling of whole landscape evolution. *Annual Review of Earth and Planetary Sciences*, 33(1), 443–459. Available from: <https://doi.org/10.1146/annurev.earth.33.092203.122610>.
- WRB. (2015) World reference base for soil resources 2014, update 2015: International soil classification system for naming soils and creating legends for soil maps. Fao Rome.
- Zhang, X., Alexander, L., Hegerl, G.C., Jones, P., Tank, A.K., Peterson, T.C. et al. (2011) Indices for monitoring changes in extremes based on daily temperature and precipitation data: Indices for monitoring changes in extremes. *WIREs Climate Change*, 2(6), 851–870. Available from: <https://doi.org/10.1002/wcc.147>.

**How to cite this article:** Rossi, M., Torri, D., De Geeter, S., Cremer, C. & Poesen, J. (2022) Topographic thresholds for gully head formation in badlands. *Earth Surface Processes and Landforms*, 47(15), 3558–3587. Available from: <https://doi.org/10.1002/esp.5473>